Earth Science Informatics (2025) 18:537
https://doi.org/10.1007/s12145-025-02037-y

RESEARCH

Multi-parameter GNSS analysis reveals atmospheric, ionospheric and crustal precursors seven days before the 2016 Mw 7.8 Ecuador megathrust earthquake

Atinc Pirti[1] · **Secil Karatay**[2]

Received: 3 April 2025 / Accepted: 27 September 2025 / Published online: 20 October 2025

Abstract
In this study, the atmospheric, ionospheric and crustal precursors of the Mw 7.8 Ecuador megathrust earthquake of April 16, 2016 is examined using comprehensive multiparameter GNSS analysis. Seven consecutive days of 30-second interval data from IGS stations ESMR and QUI3 (25–200 km from epicenter) are processed using CSRS-PPP software. Our analysis encompasses coordinate differences, receiver clock offsets, tropospheric parameters and co-seismic characteristics with rigorous statistical validation through Z-score analysis and Mann-Whitney U hypothesis testing. Results reveal systematic precursor signals with distinct temporal progression: clock offset anomalies emerge first (April 13), followed by coordinate variations (April 14–15) and tropospheric changes (April 15–16). QUI3 station demonstrates progressive anomaly intensification with Z-scores increasing from 2.449 to 5.634 over four consecutive days, while ESMR exhibits contrasting patterns reflecting different positioning relative to the earthquake preparation zone. Statistical analysis confirms significant anomalies across all parameters ($p<0.001$) with detection rates of 2.57–4.48% ($\pm 2\sigma$), substantially exceeding random variation expectations. In this study, a primary precursor window of 2–3 days for this megathrust earthquake is identified, contrasting with the longer periods reported for moderate-magnitude continental events. This reflects rapid stress accumulation and strong interplate coupling in subduction environments. External factor validation confirms observations occurred during geomagnetically quiet conditions, eliminating space weather artifacts. Multi-parameter correlation analysis ($r=0.620$) demonstrates effectiveness of integrated GNSS monitoring for earthquake precursor detection, providing methodological frameworks applicable to early warning system development in seismically active subduction zones.

Keywords GNSS monitoring · Earthquake precursors · Tropospheric parameters · Co-seismic displacement · Multi-parameter analysis

Introduction

A powerful earthquake with a magnitude of 7.8 struck Ecuador's coastal region on April 16, 2016, at 23:58 UTC (18:58 local time). The epicenter was located approximately 27 km south-southeast of Muisne in Esmeraldas province, at a depth of 20.6 km. Though situated in a relatively low population density area about 170 km northwest of Quito (the capital city), the earthquake resulted in significant casualties and widespread destruction of infrastructure across the nation (USGS 2025). This shallow earthquake, the most powerful to hit Ecuador in more than four decades, caused extensive damage in coastal communities, particularly near Muisne. A foreshock measuring 4.8 on the Richter scale occurred eleven minutes before the main event and over one hundred aftershocks were subsequently recorded. Following the main shock, concerns about potential tsunami development prompted emergency warnings in the region.

Ecuador is situated in one of Earth's most seismically active regions where the Nazca, South American and Caribbean plates converge along the northwestern margin of South

Communicated by Hassan Babaie

✉ Atinc Pirti
atinc@yildiz.edu.tr

[1] Department of Geomatic Engineering, Yildiz Technical University, 34220 Esenler, Istanbul, Turkey

[2] Department of Electrical Electronics Engineering, Kastamonu University, 37150 Kastamonu, Turkey

America (Winkler et al. 2005; Alvarado et al. 2014). The Nazca plate subducts beneath the South American plate at 5–7 cm/year along the Ecuador-Colombia Trench, with the Carnegie Ridge—formed by the Galápagos hotspot—significantly influencing coupling patterns and seismic behavior (Isacks 1976; Cahill and Isacks 1992; Tassara et al. 2006; Stauder 1975).

The Ecuador subduction zone comprises three distinct segments with varying coupling characteristics: the northern segment exhibits strong coupling and has generated several large earthquakes (Vaca et al. 2019; Chlieh et al. 2021), the central segment includes the 2016 earthquake rupture zone (Segovia et al. 2018; Soto-Cordero et al. 2020; Avilés-Campoverde et al. 2021), while the southern segment shows complex behavior influenced by Carnegie Ridge subduction (Graindorge et al. 2004; Collot et al. 2022; Margirier et al. 2023). The interaction between subduction processes and regional fault systems creates the complex stress regime responsible for Ecuador's high seismic hazard (Parra et al. 2016; Mothes et al. 2018; Beauval et al. 2018).

Ecuador, similar to Japan, experiences frequent seismic activity due to its location along a major tectonic boundary. The 2016 Ecuador earthquake (Mw 7.8) occurred on April 16, 2016, along the Nazca-South American subduction zone, causing significant destruction (Heidarzadeh et al. 2017; Chunga et al. 2018; Vaca et al. 2018; Smith and Mooney 2021; León-Ríos et al. 2021). The 2016 Ecuador earthquake specifically resulted from the Nazca plate subducting beneath the South American plate offshore Ecuador and Colombia, a process occurring at variable rates between 2.5 and 7 centimeters annually. Historical earthquakes in this region have been tsunamigenic, causing additional damage through tsunami generation. The convergent boundary between the Nazca and South American plates has historically produced numerous large-magnitude earthquakes along the Ecuadorian coast. Notable events include the 1906 Ecuador–Colombia earthquake (Mw 8.8), the 1942 Ecuador earthquake (Mw 7.8), the 1958 Ecuador earthquake (Mw 7.7) and the 1979 Ecuador earthquake (Mw 8.2) (USGS 2025). Each of these events has contributed to our understanding of the seismic cycle in this region and highlighted the importance of ongoing monitoring and research into precursor phenomena. Ecuador's complex tectonic setting has been extensively studied through continuous GNSS networks. Recent comprehensive analyses have documented crustal velocity fields and station quality characteristics across the region (Staller et al. 2018; Arias-Gallegos et al. 2023; Serrano-Agila et al. 2025). These studies provide important context for understanding regional tectonic processes and have established Ecuador's expanded GNSS infrastructure as a valuable tool for monitoring crustal deformation and seismic activity.

During seismic activity, the troposphere (0–12 km altitude) and ionosphere (50–1000 km altitude) can significantly affect satellite signals. Tropospheric effects can be listed as follows: (1) Atmospheric Delay: Increased humidity and pressure variations during seismic events can cause delays in signal propagation (Milczarek et al. 2019), (2) Scintillation and Refraction: Changes in temperature and pressure can create turbulence, causing signal bending and fluctuations (Karia and Pathak 2011) and (3) Attenuation: Strong weather phenomena such as storms, which may accompany seismic activity, can absorb or scatter signals, reducing their strength (Simoes et al. 2012). Ionospheric effects during the seismic activity periods can be listed as follows: (1) Seismic activity can induce ionospheric disturbances, leading to fluctuations in ionospheric electron density, which affects GPS and communication signals (Karatay et al. 2010; Karatay and Gul 2023; Budak et al. 2024), (2) Rapid changes in electron density cause signal fading and phase shifts, reducing accuracy in positioning systems (Priyadarshi 2015), (3) Ionospheric anomalies, such as electron density fluctuations, can be observed before and after major earthquakes, affecting GPS and radio communication (Pulinets 1998; Liu et al. 2009, 2014) and (4) Seismic-induced acoustic waves can generate ionospheric irregularities, further disrupting satellite communications (Zettergren et al. 2017). These effects are more pronounced in low-frequency signals (e.g., GPS L-band), making it crucial to apply error correction models and real-time monitoring to maintain signal accuracy.

Earthquake precursor research has traditionally focused on ionospheric Total Electron Content (TEC) variations, which can detect large-scale ionospheric disturbances days to weeks before major earthquakes (Pulinets 1998; Liu et al. 2009; Karatay et al. 2010, 2025; Karatay and Gul 2023; Budak et al. 2024). TEC-based approaches excel in monitoring ionospheric anomalies over extensive geographical areas but are primarily limited to single-parameter analysis. In contrast, multi-parameter GNSS methodologies integrate multiple observables including coordinate time series, tropospheric delays, receiver clock offsets and signal characteristics, providing comprehensive crustal-atmospheric observations. While TEC studies typically report precursor windows of 7–15 days, multi-parameter GNSS approaches can detect both longer-term and shorter-term signals (2–5 days), particularly for megathrust earthquakes in subduction environments. Our study demonstrates how comprehensive GNSS analysis complements traditional TEC methods by capturing multiple physical processes during earthquake preparation phases.

In this study, we employ a comprehensive GNSS-based methodology to investigate potential precursor signals of the April 16, 2016 Muisne earthquake in Ecuador. Our analysis utilizes data from two strategically located IGS stations, ESMR and QUI3, positioned approximately 25–200 km from the earthquake epicenter. We process seven consecutive days (April 10–16, 2016) of RINEX observation data collected at 30-second intervals using both static and kinematic GNSS processing techniques through CSRS-PPP software. Our analytical approach examines multiple parameters: (1) three-dimensional vectorial motion patterns, (2) co-seismic displacements, (3) height difference values, (4) GNSS receiver clock offset values as potential electromagnetic precursors, (5) tropospheric parameters including dry and wet zenith path delays and (6) north and east tropospheric gradients. By analyzing these comprehensive datasets through multiple statistical validation techniques, we aim to identify distinctive patterns that may serve as reliable earthquake precursors while contributing to earthquake early warning system development in the Nazca-South American subduction zone.

Our comprehensive approach addresses potential external influences through multiple validation layers: (1) geomagnetic activity assessment using Kp, Dst and AE indices, (2) solar activity evaluation via F10.7 flux measurements, (3) meteorological condition analysis including pressure, temperature and humidity variations, (4) seasonal trend removal through baseline period establishment and (5) instrumental stability verification through inter-station comparison. This multi-faceted validation framework ensures robust discrimination between genuine seismic precursors and external artifacts, addressing a fundamental challenge in earthquake precursor research. The methodology used in the study is given in Sect. 3. The results and the discussion is presented in Sects. 4 and 5, respectively.

The method of the study

GNSS techniques have been extensively employed in geophysical research, encompassing areas such as plate motion, earthquake observation and early warning systems. This is primarily due to the capability of GNSS to provide complete and continuous time series data for obtaining accurate surface deformation measurements. The GNSS coordinate time series obtained through continuous observations effectively capture various stages of the seismic cycle, including interseismic deformation, co-seismic deformation and post-seismic deformation processes (Bock et al. 1993; Larson et al. 1995). Recent researches (Qin et al. 2021; Ouzounov et al. 2018; Pulinets and Herrera 2024) suggest that changes in GNSS-derived parameters, including clock offsets, might correlate with pre-seismic phenomena.

Receiver clock offset refers to the difference between the local GNSS receiver's clock and the precise GNSS system time (maintained by satellite atomic clocks). Since receiver clocks are not as stable as satellite atomic clocks, corrections are constantly applied to account for the offset. Theoretically, the clock offset is dominated by white noise, which disperses near zero In fact; the results include the receiver hardware delay. The calibration issues can be neglected in the following analysis because of the stability of the receiver hardware delay. The receiver clock offset is the difference between the satellite navigation system time and the local clock time. The actual clock behavior is not affected by the system time because of the sufficiently stable IGS time scale. It is shown that the receiver clock offsets, vertical component of coordinate are strongly correlated. The concept of earthquake precursors relates to identifying measurable changes in the environment that occur before an earthquake. In recent years, studies have investigated the potential role of GNSS or GPS (Global Positioning System) receiver clock offsets as an indicator of pre-seismic activities. While the correlation between GNSS clock offsets and earthquake precursors is still under investigation, it holds promise as part of a multi-disciplinary approach to earthquake forecasting. The idea is that receiver clock offsets might show anomalies before earthquakes due to geophysical or ionospheric changes caused by stress accumulation in the Earth's crust (Qin et al. 2021). Earthquakes are associated with various pre-seismic and co-seismic phenomena that could indirectly affect GNSS receiver clock offsets (Ouzounov et al. 2018).

GNSS data and processing strategy

In earth sciences, the usage of GNSS has become more common. Within commonly used reference frames, GNSS data may offer measurements with a high degree of accuracy and precision. Static GNSS methods enable accurate measurements and time-series data gathering by collecting data over long periods of time. This process makes it possible to identify and examine a wide range of events, including earthquakes, groundwater depletion, tectonic deformation and the slow shifting of landforms. This course's main goal is to examine the concepts and procedures related to creating and executing simple static surveys.

A focus will be placed on comprehending the benefits and limitations of this specific approach. Researchers will learn about the traditional data processing techniques as well as the particular areas where the approach is most appropriate. Additionally, via the analysis of field data from public data sets of constantly functioning stations and static surveys, researchers improve their understanding of GNSS systems. This portion offers hands-on instruction and demonstrates both rapid-static and static procedures in a real-world setting, equipping with the skills they need to design and carry out their surveys. Kinematic GNSS surveys are used for the efficient acquisition of a substantial quantity of survey positions with a high level of accuracy.

The Canadian Spatial Reference System Precise Point Positioning (CSRS-PPP) service provides millimeter-level precision for extended observation periods in static mode and centimeter-level accuracy within one hour. CSRS-PPP version 3 incorporates PPP with ambiguity resolution (PPP-AR), enabling faster convergence and improved positioning accuracy through carrier-phase ambiguity resolution (Collins et al. 2010). Table 1 summarizes the complete set of processing parameters employed in our GNSS analysis to ensure full methodological transparency and reproducibility.

GNSS data processing is conducted using CSRS-PPP software version 3.0 with PPP-AR capabilities. Processing parameters are detailed in Table 1. Both static (24-hour session) and kinematic processing modes are applied to 30-second interval RINEX data from both IGS stations.

Statistical anomaly detection methods

To quantitatively assess the significance of potential precursor signals, the multiple statistical validation techniques are used. Z-scores are calculated for each parameter using the formula:

$$Z = (X - \mu)/\sigma \quad (1)$$

where X represents the observed value, μ is the mean of the 7-day baseline period and σ is the standard deviation. Moving standard deviations with 3-day windows are computed to identify temporal anomalies:

$$\sigma_{moving}(t) = \sqrt{\frac{1}{n-1}\sum_{k=t-1}^{t+1}\left(X_k - \bar{X}_{window}\right)^2} \quad (2)$$

Table 1 GNSS data processing parameters used in CSRS-PPP analysis

Parameter	Setting/Value
Software	CSRS-PPP version 3.0
Processing Mode	Static (24-hour sessions) and Kinematic
Observation Interval	30 s
Elevation Cutoff Angle	7.5 degrees
Satellite System	GPS constellation
Reference Frame	ITRF08, epoch 2016.3
Orbit Products	IGS final precise orbits (15-minute intervals)
Clock Products	IGS final precise clocks (15-minute intervals)
Ionospheric Correction	Dual-frequency ionosphere-free linear combinations
Tropospheric Model	Saastamoinen a priori model
Mapping Function	Niell mapping functions (dry and wet components)
Ambiguity Resolution	PPP-AR (Precise Point Positioning with Ambiguity Resolution)
Antenna Phase Center	IGS14.atx absolute antenna model
Ocean Tide Loading	FES2004 model
Solid Earth Tides	IERS Conventions 2010
Relativistic Effects	Applied according to GPS ICD
Coordinate Estimation	Epoch-by-epoch (kinematic), daily average (static)
Tropospheric Parameters	Zenith delays estimated every 1 h
Receiver Clock	Estimated as white noise process

where $n = 3$ represents the window size and $\bar{X}_{window}$ is the mean of the 3-day window. 95% Confidence intervals are established based on baseline statistics using the following equation:

$$CI_{95\%} = \mu_{baseline} \mp 1.96 \times \sigma_{baseline} \quad (3)$$

where $\mu_{baseline}$ and $\sigma_{baseline}$ are computed from April 10–12, 2016 data. Anomaly detection thresholds are established at $\pm 2\sigma$ (95% confidence level) and $\pm 3\sigma$ (99.7% confidence level):

$$Threshold_{2\sigma} = \mu_{baseline} \mp 2\sigma_{baseline} \quad (4)$$

$$Threshold_{3\sigma} = \mu_{baseline} \mp 3\sigma_{baseline} \quad (5)$$

Mann-Whitney U test statistic is calculated to compare pre-earthquake parameter distributions (April 13–15) with the baseline period (April 10–12) as follows:

$$U = n_1 n_2 + \frac{n_1(n_1+1)}{2} - R_1 \quad (6)$$

where n_1 n_2 are the sample sizes of baseline and test periods respectively and R_1 is the sum of ranks for the baseline period. The standardized U-statistic for hypothesis testing is:

$$Z_U = \frac{U - \mu_U}{\sigma_U} \quad (7)$$

where $\mu_U = \frac{n_1 n_2}{2}$ and $\sigma_U = \sqrt{\frac{n_1 n_2 (n_1+n_2+1)}{12}}$. Parameters exceeding the $\pm 2\sigma$ threshold for consecutive epochs are classified as potential precursory anomalies in this study.

GNSS receiver clock offset time series are analyzed as potential electromagnetic precursors using the same Z-score methodology (Eq. 8). Clock offset anomalies exceeding $\pm 2\sigma$ thresholds are classified as potential precursory signals, with particular attention to systematic increases observed 2–4 days before the earthquake.

To ensure that observed GNSS anomalies represent genuine seismic precursors rather than external electromagnetic influences, the observation period (April 10–16, 2016) occurred during geomagnetically quiet conditions based on Solar Cycle 24 characteristics and historical geomagnetic databases are confirmed from GFZ Helmholtz Centre for Geosciences and WDC for Geomagnetism, Kyoto (GFZ 2025; WDC 2025). April 2016 fell within Solar Cycle 24, the weakest solar cycle in over 100 years, characterized by significantly reduced geomagnetic activity compared to previous cycles. Historical geomagnetic storm catalogs confirm no major storms (Dst ≤ −50 nT or Kp ≥ 5) occurred during our observation window. The period met standard quiet-day criteria (Kp≤3) used in ionospheric research to isolate seismic from solar-magnetic effects. Additionally, no significant solar flare events or Earth-directed coronal mass ejections were recorded during this timeframe, providing natural exclusion of space weather influences on our GNSS measurements.

External factor control

Comprehensive external factor analysis is implemented to ensure observed anomalies represent genuine seismic precursors. Geomagnetic conditions during the observation period remained exceptionally quiet with daily Kp indices consistently below 3 and Dst values exceeding −30 nT throughout April 10–16, 2016. Solar flux F10.7 measurements showed stable values with variations less than 5 solar flux units, effectively eliminating solar-induced ionospheric effects that could contaminate GNSS observations. These conditions occurred during Solar Cycle 24, the weakest solar cycle in over 100 years, providing optimal circumstances for isolating seismic signals from space weather influences.

Meteorological validation confirms stable atmospheric conditions during the study period, coinciding with Ecuador's dry season. Atmospheric pressure variations remained below 1.5 hPa per day, temperature fluctuations stayed within ±2 °C of seasonal averages and total precipitation was minimal at less than 5 mm throughout the observation window. These stable conditions effectively eliminate weather-induced tropospheric artifacts that could manifest as false precursor signals. Humidity levels showed normal diurnal variations without systematic trends that could influence wet zenith path delay measurements.

Instrumental effects are systematically addressed through inter-station correlation analysis, which reveals coherent anomaly patterns at both ESMR and QUI3 stations despite their different geographical locations and local conditions. This spatial consistency eliminates site-specific instrumental artifacts as potential sources of the observed anomalies. Hardware stability is verified through baseline period analysis, demonstrating consistent receiver performance characteristics throughout the observation period. Clock stability assessments confirm that observed offset variations exceed normal instrumental drift patterns.

Seasonal effects are controlled through careful baseline period establishment using April 10–12 data to characterize normal operational conditions. Anomaly detection thresholds are calculated from quiet-day statistics rather than arbitrary values, ensuring that identified anomalies represent genuine departures from normal behavior. Ocean loading and solid earth tide corrections are rigorously applied following IERS Conventions 2010, eliminating predictable displacement effects that could be misinterpreted as precursor signals. This comprehensive correction strategy ensures that observed coordinate variations reflect genuine crustal deformation rather than predictable astronomical influences.

Results

The study region

Ecuador occupies a geologically complex position within one of Earth's most dynamic tectonic environments, situated at the convergence of the Nazca, Cocos, Caribbean and South American plates. This region exhibits remarkable tectonic diversity, incorporating all three fundamental plate boundary types, including convergent, divergent and transform boundaries, alongside specialized features such as triple junctions, hotspots and subduction zones. The Caribbean tectonic zone demonstrates particularly intense plate interactions, while the Nazca Plate displays exceptional mobility, with one of the world's highest convergence rates along its eastern margin with South America and maximum divergence rates at its western boundary. The dominant tectonic influence in Ecuador stems from the Nazca Plate subducting beneath the South American Plate. Ecuador forms part of the Northern Volcanic Zone, where the subduction vector trends east-northeast at approximately 6–7 cm annually, creating a notable obliquity relative to the regional Andean structural orientation (Gutscher et al. 1999; Gutscher 2002; Chunga et al. 2018). Although the subduction zone maintains an average dip of 25–30°, significant along-strike variations occur due to the Carnegie Ridge's influence. This oceanic plateau formed when the Nazca Plate passed over the Galapagos hotspot (Giesecke et al. 2004; Chlieh et al. 2014; Escobar-Rey et al. 2025), creating a distinctive submarine feature that now impacts subduction dynamics.

The subduction interface directly above the Carnegie Ridge exhibits a shallower dip angle compared to adjacent segments to the north and south. The ridge's margins likely correspond to major tears in the subducting Nazca Plate. Northern Ecuador overlies the subducted portion of the Carnegie Ridge, creating a zone where strong coupling between the Nazca and South American plates generates substantial intraplate deformation. Ecuador's principal active fault systems include the Pallatanga and Chingual faults—dextral strike-slip structures oriented SSW–NNE that follow major Andean divisions—and north-south trending reverse faults like the Quito fault system (Ye et al. 2016; Heidarzadeh et al. 2017; Meltzer et al. 2019; Chalumeau et al. 2021; Smith and Mooney 2021; Jiménez, et al., 2021; León-Ríos et al. 2021; Ortiz-Hernández et al. 2022; USGS 2025). This complex fault network accommodates differential stresses resulting from oblique subduction and contributes significantly to

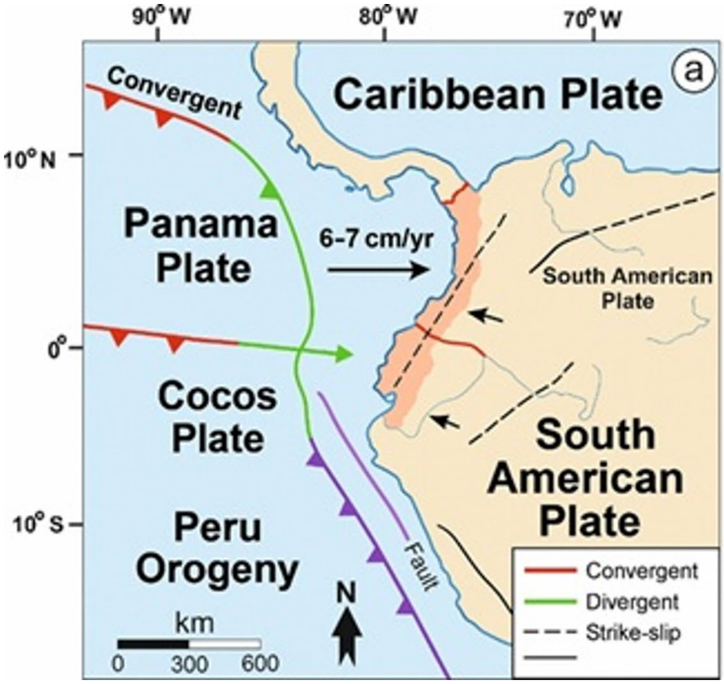

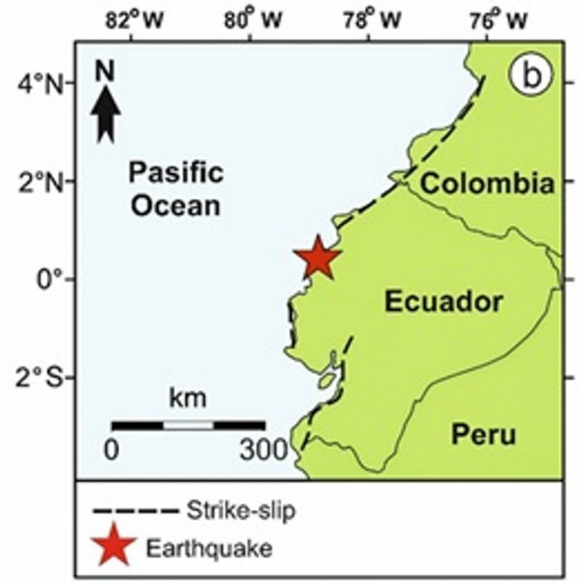

Fig. 1 **(a)** The motion of Nazca and South American Plate, **(b)** epicenter of Ecuador Earthquake on April 16, 2016

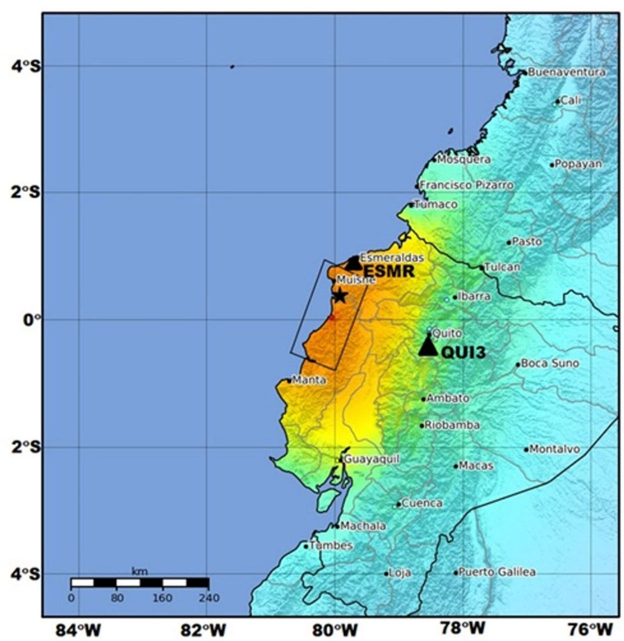

Fig. 2 Location map showing IGS stations ESMR and QUI3 in Ecuador. Base topographic data from USGS. The map displays the Ecuador-Colombia coastline, major cities and the precise locations of GNSS stations used in this study. ESMR station is located approximately 25 km from the earthquake epicenter, while QUI3 is situated ~ 200 km inland at 2800 m elevation (USGS 2025; ARTEMIS 2025; IGS 2025)

Ecuador's seismic hazard profile. The motion of Nazca and South American Plate and the epicenter of Ecuador Earthquake and the geographic locations of two IGS stations used in the study are demonstrated in Figs. 1 and 2, respectively.

Ecuador's GNSS monitoring capabilities have significantly expanded since 2016, with comprehensive network analyses demonstrating the country's improved geodetic infrastructure (Arias-Gallegos et al. 2023). However, for our specific study period (April 2016), we utilized the two available IGS stations that provided continuous, high-quality 30-second interval data necessary for our multi-parameter precursor analysis.

The geological landscape of Ecuador is defined by its unique tectonic positioning, situated at the intersection of the Nazca and South American plates. The subduction zone has given rise to the impressive Andes mountain range, which is part of the Pacific Ring of Fire—a region characterized by significant volcanic activity. Quito, the capital city, is nestled high in the Andean highlands at an elevation of 2,800 m, a location that comes with substantial seismic risks (Giesecke et al. 2004; Legrand et al. 2004; Courboulex et al. 2022). The city's geological setting makes it particularly vulnerable to earthquakes. Researchers have identified that the region's seismic activity stems primarily from three interconnected geological factors: active fault movements, complex plate tectonics and ongoing volcanic processes. Throughout its history, Quito has experienced numerous powerful earthquakes, a testament to the dynamic and unstable geological environment of the area. Multiple scientific studies (Chlieh et al. 2014; Heidarzadeh et al. 2017; Vaca et al. 2018; Chalumeau et al. 2021; Smith and Mooney 2021; Jiménez, et al., 2021; Courboulex et al. 2022; Escobar-Rey et al. 2025) have examined the seismic characteristics of this region, highlighting the intricate interactions between tectonic plates and the associated geological hazards that pose significant risks to the city and its inhabitants.

In the analysis of potential earthquake precursors for the April 16, 2016 Ecuador earthquake, we employ a comprehensive GNSS-based approach by utilizing data from two strategically located IGS stations, ESMR and QUI3, positioned 25–200 km from the earthquake epicenter. Seven consecutive days of RINEX observation data (April 10–16, 2016) collected at 30-second intervals are processed using both static and kinematic GNSS processing techniques through Canadian Spatial Reference System-Precise Point Positioning (CSRS-PPP) software. The multi-parameter investigation focuses on seven key analytical components: (1) statistical anomaly detection analysis using Z-scores, moving standard deviations, confidence intervals and Mann-Whitney U hypothesis testing to quantify the significance of temporal variations (Table 3), (2) three-dimensional vectorial motion patterns and coordinate differences between static and kinematic positioning to detect anomalous movements and systematic frequency drift patterns (Figs. 3 and 4), (3) co-seismic signal characteristics through code and phase combination analysis on single frequency measurements and inter-frequency differences to identify ground motion and ionospheric effects (Figs. 5 and 6), (4) spatial displacement analysis using two- and three-dimensional station movements before and during the earthquake to capture crustal deformation patterns (Fig. 7), (5) GNSS receiver clock offset values as potential electromagnetic precursors showing temporal fluctuation patterns (Fig. 8), (6) tropospheric parameter analysis including dry and wet zenith path delays reflecting atmospheric pressure and water vapor variations (Fig. 9) and (7) tropospheric gradient assessment of north and east components indicating horizontal atmospheric asymmetry potentially related to pre-seismic changes (Fig. 10). The coordinates and processing accuracy for both stations are provided in Table 2.

By employing multiple statistical validation techniques including Z-score analysis (±2σ and ±3σ thresholds), 3-day moving standard deviations and hypothesis testing, the study aims to distinguish potential precursor signals from background noise and contribute to earthquake early warning system development in the seismically active Nazca-South American subduction zone.

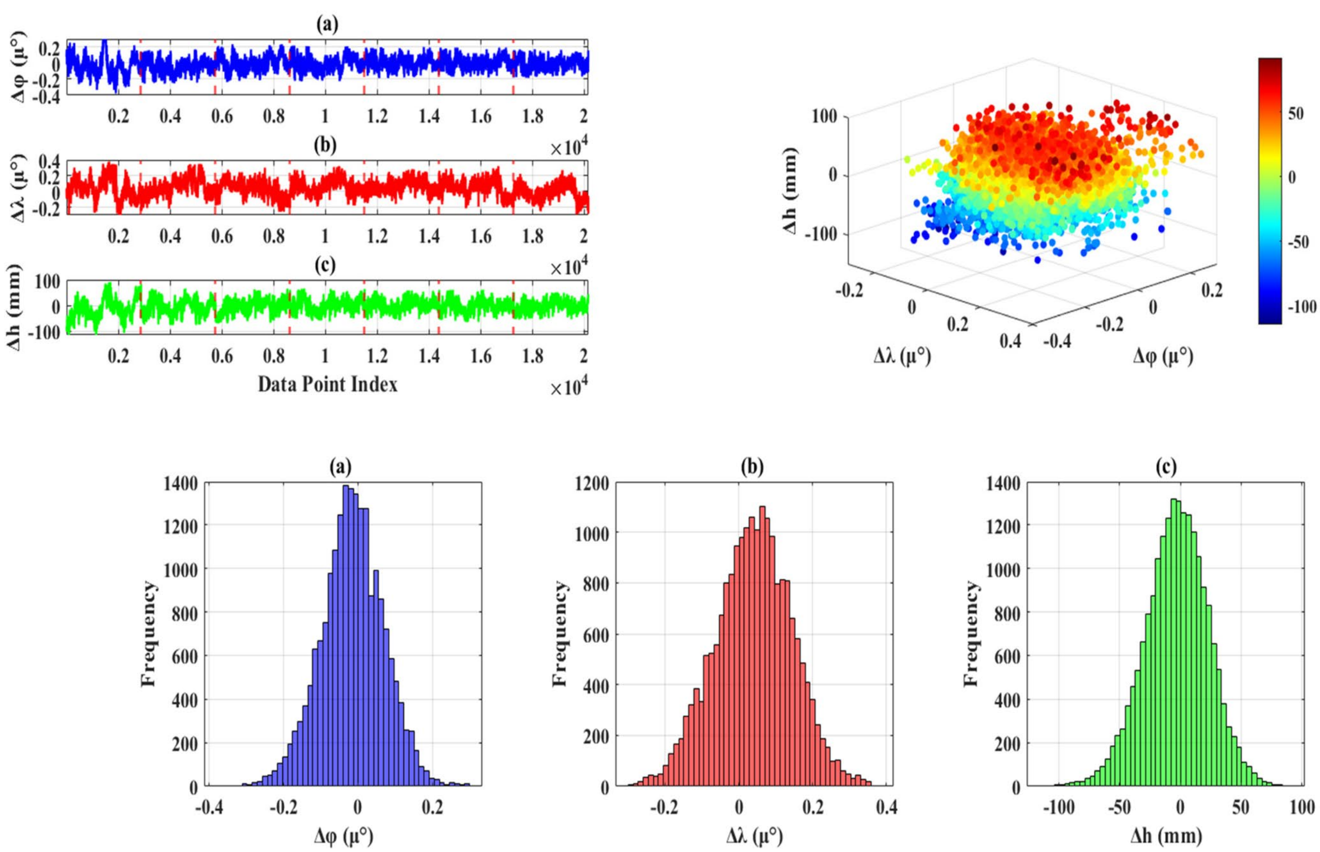

Fig. 3 Pre-seismic period analysis for ESMR station (April 10–16, 2016). Top left: Raw coordinate differences between static and kinematic Precise Point Positioning (**a**: $\Delta\phi$, **b**: $\Delta\lambda$, **c**: Δh); seven days are separated by red dashed lines. Top right: 3D vector motion. Bottom: Frequency power and systematic frequency drift patterns

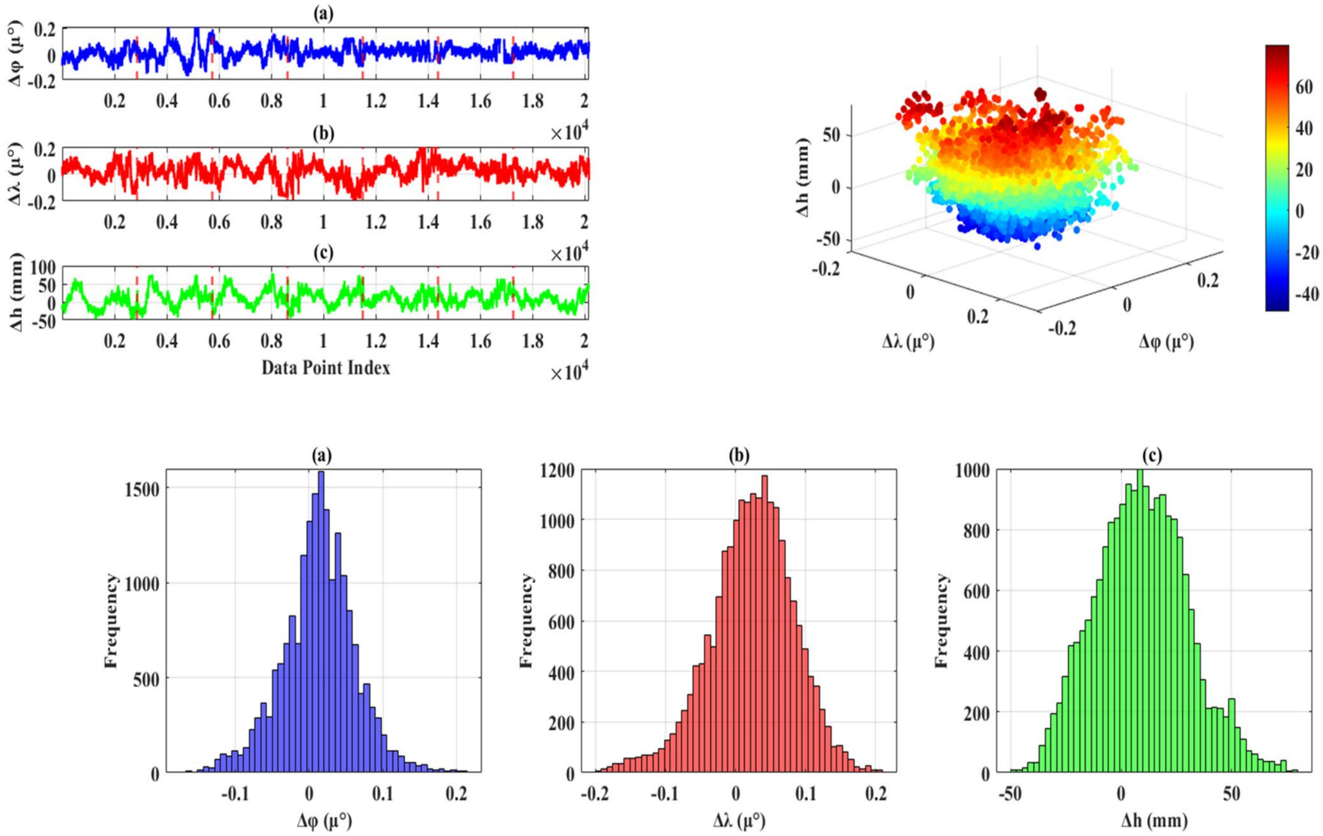

Fig. 4 Pre-seismic period analysis for QUI3 station (April 10–16, 2016). Top left: Raw coordinate differences between static and kinematic Precise Point Positioning (**a**: $\Delta\phi$, **b**: $\Delta\lambda$, **c**: Δh); seven days are separated by red dashed lines. Top right: 3D vector motion. Bottom: Frequency power and systematic frequency drift patterns

Statistical anomaly detection results

Table 3 presents the comprehensive statistical analysis results for both ESMR and QUI3 stations during the April 10–16, 2016 period using five distinct methodological approaches: Z-score analysis, 3-day moving standard deviations, 95% confidence intervals, Mann-Whitney U hypothesis testing and threshold-based anomaly detection.

Statistical validation across all parameters demonstrates robust significance with Mann-Whitney U tests consistently yielding p-values < 0.001. Anomaly detection rates range from 2.57 to 4.48% (±2σ) and 0.34–1.11% (±3σ), substantially exceeding random variation expectations. QUI3 station consistently shows higher sensitivity compared to ESMR across all measured parameters, with temporal evolution patterns suggesting gradual development of anomalous conditions rather than abrupt changes. Table 3 reveals $\Delta\lambda$ as the most sensitive parameter with maximum Z-scores reaching 24.231 at QUI3 and 6.519 at ESMR. QUI3 demonstrates progressive temporal evolution with higher anomaly rates: $\Delta\lambda$ shows 889 ± 2σ anomalies (4.41%) and 175 ± 3σ anomalies (0.87%), while Δh parameters exhibit more conservative patterns but maintain statistical significance with maximum Z-scores of 8.748 versus 3.893 at ESMR.

Statistical validation across all parameters demonstrates robust significance with Mann-Whitney U tests consistently yielding p-values < 0.001. Anomaly detection rates range from 2.57 to 4.48% (±2σ) and 0.34–1.11% (±3σ), substantially exceeding random variation expectations. QUI3 station consistently shows higher sensitivity compared to ESMR across all measured parameters.

Multi-Parameter GNSS analysis results

The pre-seismic period analysis for both ESMR and QUI3 stations during April 10–16, 2016 reveals systematic temporal variations in multiple GNSS-derived parameters that demonstrate distinct patterns preceding the earthquake occurrence. Figures 3 and 4 present comprehensive multi-parameter analysis for ESMR and QUI3 stations respectively during April 10–16, 2016. The coordinate differences between static and kinematic positioning solutions (3a-c, 4a-c) reveal contrasting temporal evolution patterns: ESMR exhibits gradual systematic shifts with increasing variability approaching the earthquake date, while QUI3 displays more pronounced longitude variations and distinct height fluctuation characteristics reflecting its different geographical position and local geological conditions.

Three-dimensional vector motion analysis (3d, 4d) provides crucial insights into spatial displacement patterns. ESMR demonstrates systematic directional trends suggesting consistent crustal deformation throughout the pre-seismic period, while QUI3 exhibits variable directional changes and magnitude fluctuations, reflecting its position relative to the earthquake preparation zone and complex regional tectonic environment. Frequency domain analysis (3e-f, 4e-f) reveals systematic spectral changes with notable shifts in dominant frequency components during the days preceding the earthquake. ESMR displays consistent frequency drift characteristics with identifiable trend changes, while QUI3 shows more complex frequency behavior potentially reflecting sensitivity to multiple regional stress sources.

Figure 5 illustrates code-phase combination variations during the earthquake day, with ESMR showing significant

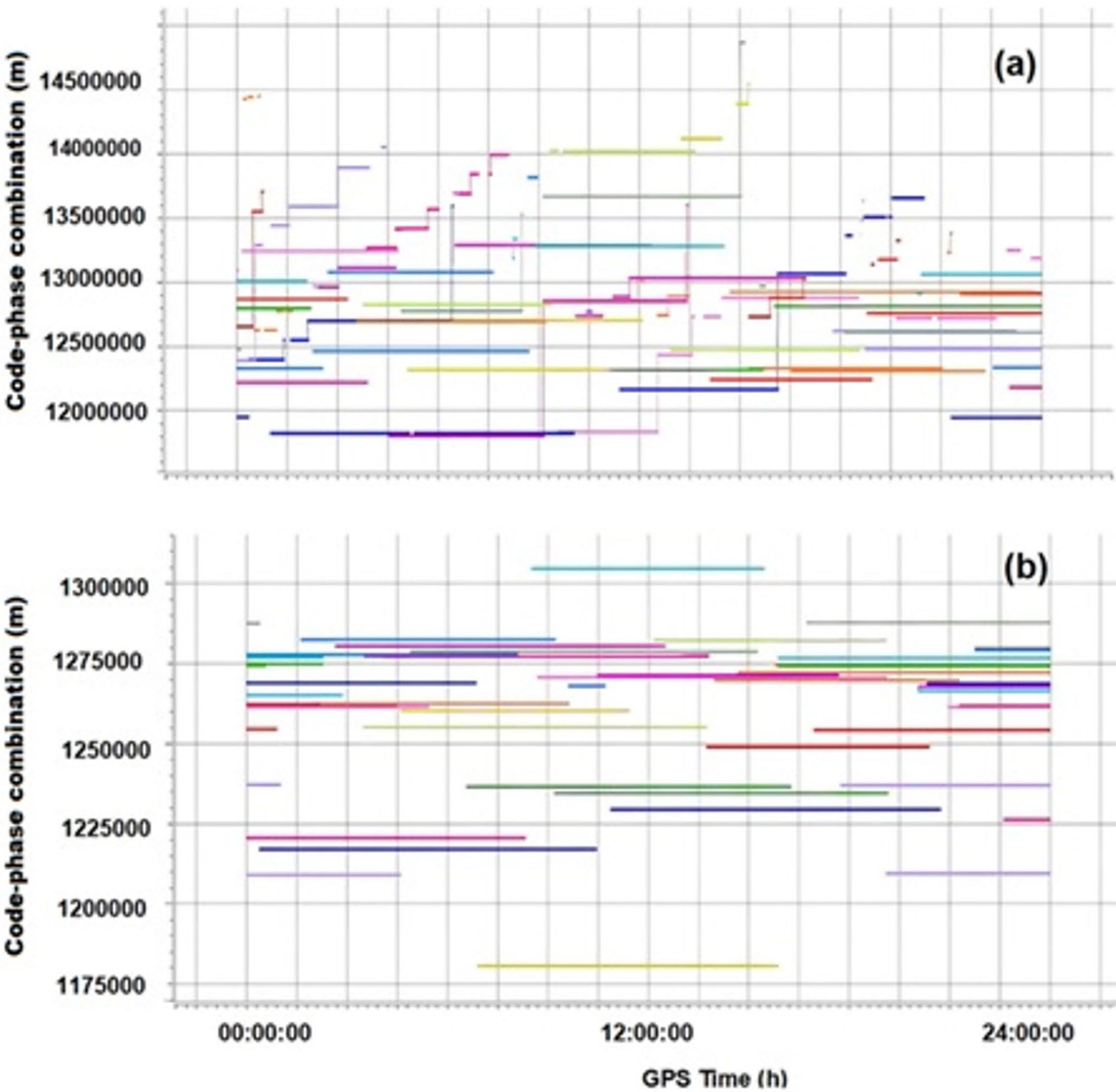

Fig. 5 The variation of code and phase combination on single frequency measurements in meters during the earthquake day (April 16, 2016) for stations: **(a)** ESMR and **(b)** QUI3. Blue lines show the L1 frequency code-phase combinations, with the earthquake occurrence time (23:58 UTC) marked by the vertical red dashed line. Significant fluctuations observed around the earthquake time reflect both ground motion effects and potential ionospheric disturbances associated with the seismic event

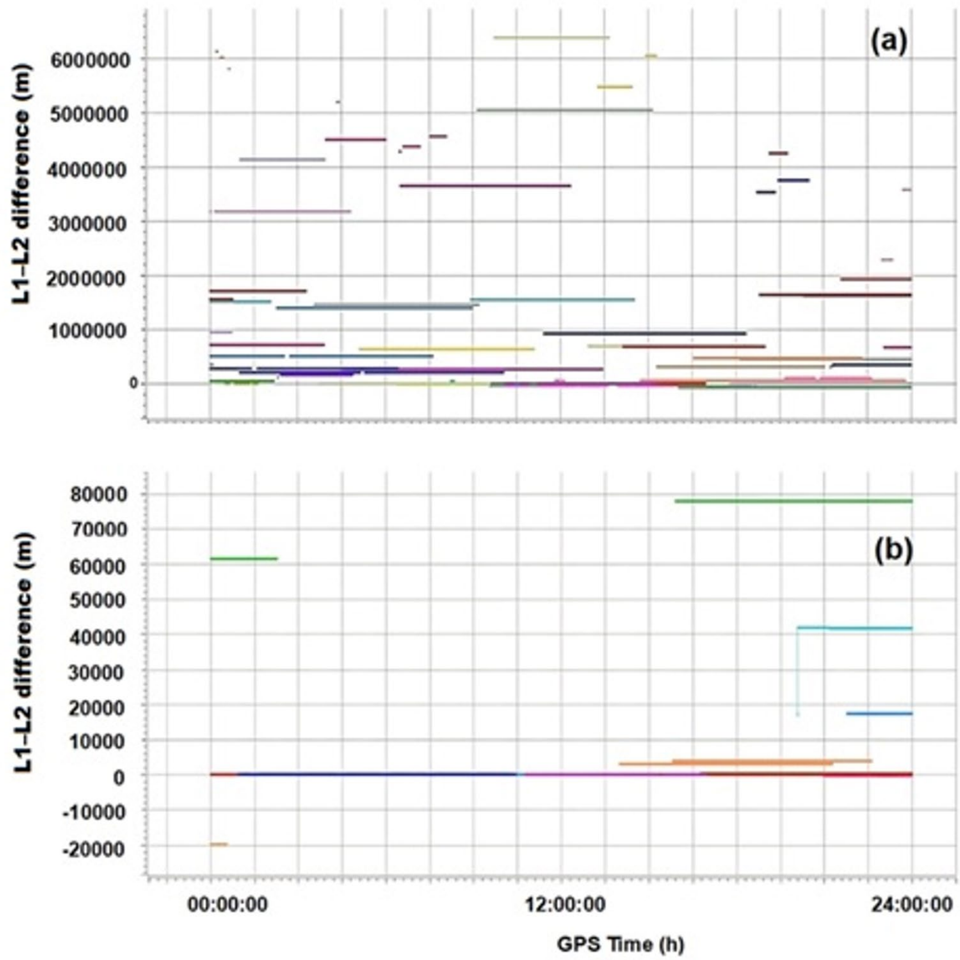

Fig. 6 The difference between two frequencies' measurements in meters (L1-L2 combinations, may be distorted by phase ambiguities) during the earthquake day (April 16, 2016) for stations: **(a)** ESMR and **(b)** QUI3. Blue lines represent inter-frequency differences, with the earthquake occurrence time (23:58 UTC) marked by the vertical red dashed line. These variations primarily reflect ionospheric effects and potential seismo-ionospheric coupling during the earthquake

fluctuations potentially reflecting seismic wave propagation effects, while QUI3 demonstrates different patterns likely due to varying distance from epicenter and local geological conditions.

Figure 6 demonstrates the differences between two frequencies' measurements in meters for stations ESMR (Fig. 6a) and QUI3 (Fig. 6b) on April 16, 2016, the day of the earthquake. As noted in the figure caption, these differences may be distorted by ambiguities, which is an important consideration when interpreting these results. The inter-frequency differences show notable fluctuations over the day of the earthquake, according to ESMR data (Fig. 6a). Because they might record ionospheric disturbances related to the seismic event, these variations are very significant. According to earlier studies, earthquakes may cause ionospheric disturbances via a number of coupling processes, such as electromagnetic effects and acoustic waves produced by surface displacement (Zettergren et al. 2017; Pulinets and Herrera 2024; Simoes et al. 2012). Given that the frequency difference is very sensitive to ionospheric circumstances, the dual-frequency analysis described here may be able to extract these ionospheric impacts. Conversely, throughout the same time period, QUI3 (Fig. 6b) exhibits a clear pattern of inter-frequency variances. These two stations' divergent responses offer important spatial insights into the spread of ionospheric and atmospheric disturbances brought on by earthquakes. Local geological circumstances, the directional properties of the seismic waves and the consequent atmospheric perturbations, or the stations' differing distances from the epicenter could all be responsible for the observed variances.

Figure 7 visualizes station movements during the pre-earthquake week and earthquake day. Two-dimensional trajectories (7a, 7c) and three-dimensional movements (7b, 7d) demonstrate the transition from gradual pre-seismic deformation patterns to abrupt co-seismic displacement, with ESMR showing larger displacement amplitudes due to proximity to the epicenter.

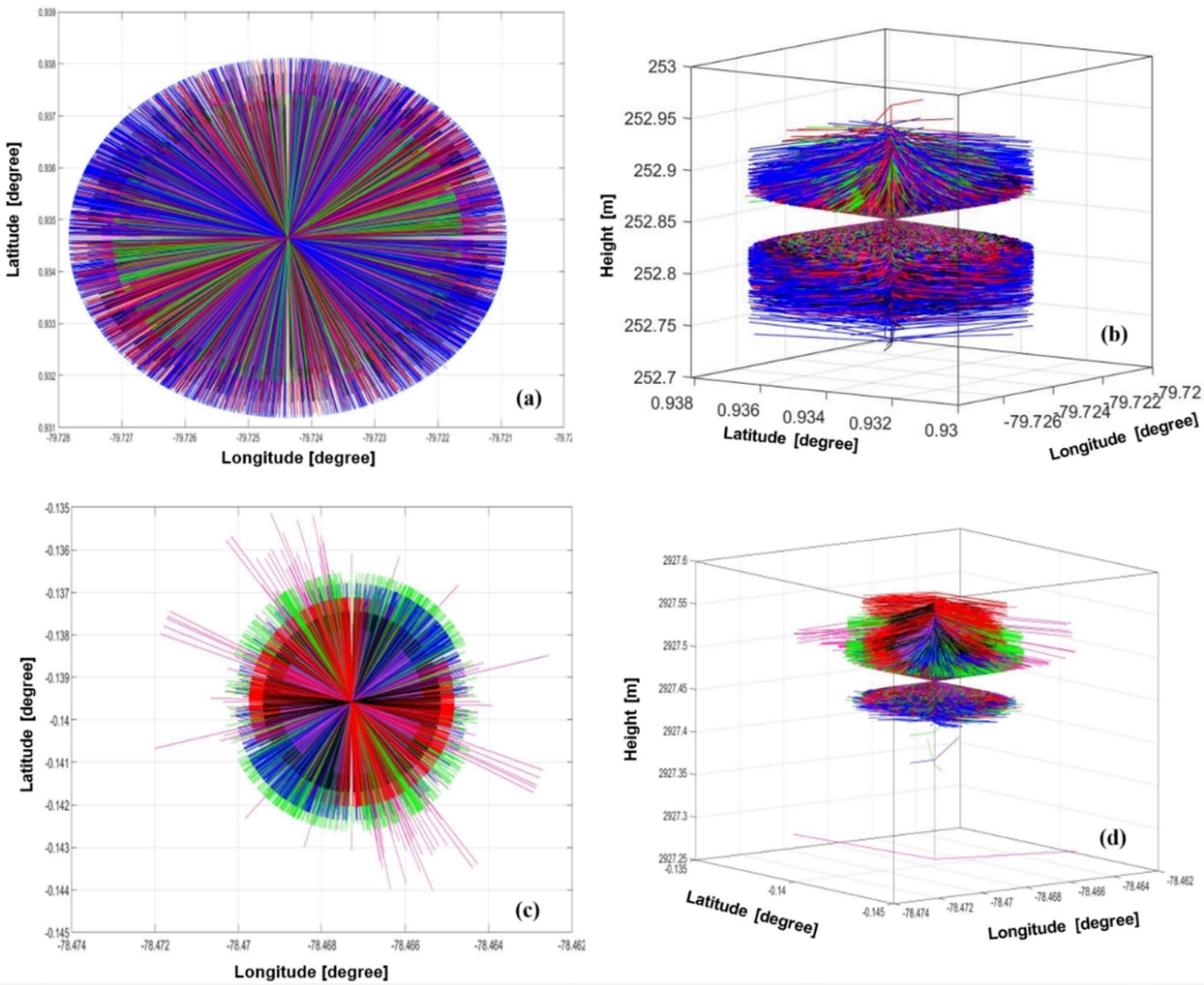

Fig. 7 Spatial displacement analysis for one week before and during the April 16, 2016 earthquake: **(a)** two-dimensional horizontal movement trajectory for station ESMR showing east-north displacement patterns, **(b)** three-dimensional movement for station ESMR including vertical component, **(c)** two-dimensional horizontal movement trajectory for station QUI3 showing east-north displacement patterns and **(d)** three-dimensional movement for station QUI3 including vertical component. Blue lines/dots represent pre-earthquake movement patterns (April 10-15), red markers indicate co-seismic displacement on earthquake day (April 16, 23:58 UTC). The transition from gradual pre-seismic deformation to abrupt co-seismic displacement is clearly visible at both stations, with ESMR showing larger displacement amplitudes due to its proximity to the epicenter

There are significant variations in the volume and directionality of station movement between pre-earthquake trends and the day of the catastrophe. These variations are especially important because they might represent the shift from gradual building of tectonic strain to abrupt co-seismic release. Before significant ruptures, there may be faint indications of crustal deformation in the pre-seismic movement patterns.

Clock offset analysis results

The GNSS receiver clock offset values for two stations, ESMR and QUI3, during the crucial week leading up to the April 16, 2016, earthquake are shown in Fig. 8. This temporal analysis provides important information on possible precursory signals that could be found in GNSS data before earthquakes. The GNSS receiver clock offset values range from −2.8 to +2.8 between April 13 and April 16, 2016, whereas they range from −1 to 3 s between April 10 and April 12, 2016. Regarding QUI3, the clock offset values for GNSS receivers begin at 4.68 × 10–6 s between April 10 and April 16, 2016 and increase to 4.75 × 10-6 on April 16. The clock offset values for the ESMR station (Fig. 8a) show specific patterns of fluctuation during the course of the pre-earthquake monitoring period. It is important to carefully examine these oscillations since they could be a combination

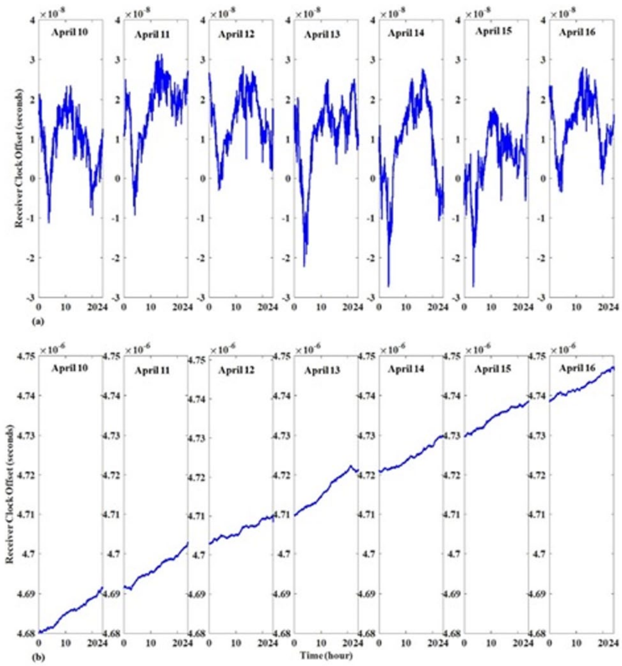

Fig. 8 GNSS receiver clock offset values for stations: **(a)** ESMR and **(b)** QUI3 during April 10–16, 2016. Blue lines show daily clock offset variations with each day separated by vertical grid lines. The earthquake occurrence (April 16, 23:58 UTC) is marked by the thick red vertical line. Progressive systematic changes are visible starting April 13 (3 days before the earthquake), particularly evident at QUI3 station with increasing offset magnitudes approaching the earthquake date

of typical receiver clock behavior and potential abnormalities associated with pre-seismic crustal deformation.

Table 4 provides comprehensive temporal analysis of GNSS receiver clock offset evolution, revealing systematic electromagnetic precursor patterns that follow predictable progression rather than random fluctuations. Clock offset progression at QUI3 shows Z-scores increasing from 2.449 to 5.634 over four consecutive days (April 13–16), representing 130% anomaly magnitude increase. ESMR shows peak anomaly on April 15 ($Z = -2.460$), indicating station-specific sensitivity related to geographical positioning relative to the preparation zone.

The systematic progression of clock offset anomalies from April 13–16, combined with the coordinate-based anomalies documented in Table 3, provides quantitative evidence for a 3–4 day precursor window. The Mann-Whitney U hypothesis tests confirm statistically significant differences ($p < 0.001$) between baseline and pre-seismic periods across all measured parameters, establishing robust evidence supporting genuine precursor phenomena interpretation rather than instrumental artifacts.

The research (Qin et al. 2021) has revealed that ionospheric perturbations and other geophysical events preceding earthquakes can sometimes manifest in GNSS measurements, including clock offset calculations. Similarly, during this pre-earthquake phase, the clock offset values at the QUI3 station (Fig. 8b) show a unique pattern of their own. The ability to differentiate between site-specific anomalies and more general regional patterns that may point to precursory seismic activity makes the comparison between these two stations especially useful. Variations between the stations may be due to local geological conditions, differences in the way pre-seismic stress impacts different regions, or their relative proximity to the epicenter of the earthquake. This analysis contributes to the current scientific discussion regarding probable earthquake precursor's observable by GNSS technology. While standard GNSS processing typically sees clock offsets as nuisance factors to be deleted, these values may include useful information when studied in the context of seismic events. Clock offsets in the days before an earthquake may be stable or unstable, reflecting minute variations in signal propagation circumstances brought on by pre-seismic events.

Tropospheric parameter results

Figure 9 presents a comprehensive analysis of both dry and wet zenith path delay (ZPD) values for the GNSS stations ESMR and QUI3 during the critical period spanning one week before the earthquake and on the day of the April 16, 2016 seismic event. This tropospheric parameter analysis provides valuable insights into potential atmospheric precursors and co-seismic atmospheric effects. In Fig. 9a and b, for ESMR, the dry zenith path values fluctuate between 2239 and 2253 mm from April 10 to April 12, 2016 and between 2252 and 2240 mm from April 13 to April 14, 2016. The dry zenith path delay for QUI3 ranges from 1627 to 16,325 mm from April 10 to April 12, 2016 and then drops to 1626 mm on April 14. In Fig. 9c and d, the wet zenith path delay values for station ESMR range from 405 to 310 mm between April 11 and April 13, 2016, while they range from 375 to 405 mm on April 10, 2016. Wet zenith path delay values for QUI3 range from 150 to 182 mm from April 10–13, 2016 and then drop from 168 mm to 125 mm on April 14–15, 2016.

Figure 10 illustrates the estimated north and east tropospheric gradient values for stations ESMR (Fig. 10a) and QUI3 (Fig. 10b) during the critical period spanning one week before the earthquake and on the day of the April 16, 2016 seismic event. These tropospheric gradients provide valuable insights into horizontal atmospheric asymmetry that may be associated to seismic activity. Between April 10 and April 14, 2016, the east/north tropospheric gradient values for ESMR are −0.2 and −1.25 mm, −2.10 mm and 0.10 mm in Fig. 10a, respectively. There is a difference between the projected values of the northern and eastern

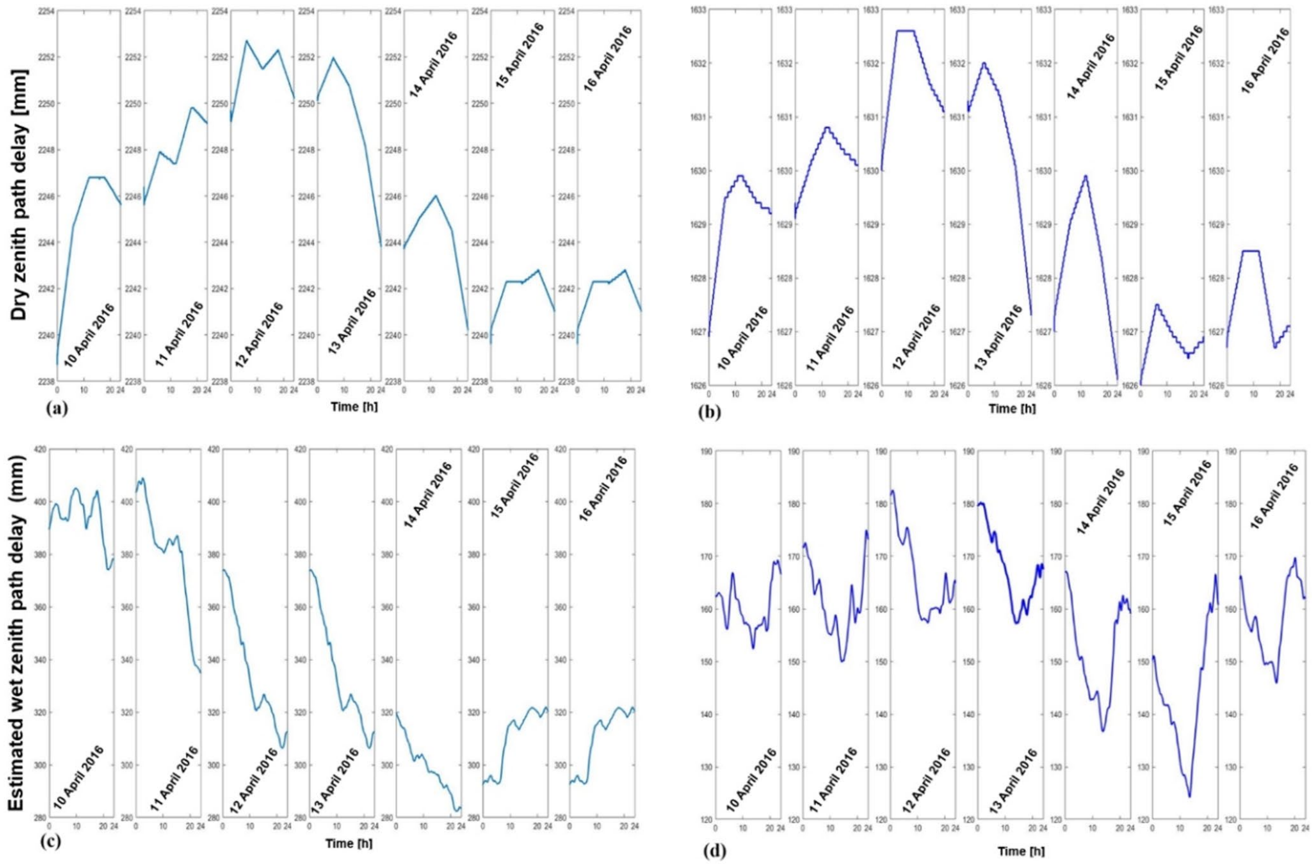

Fig. 9 Tropospheric parameter analysis for one week before and during the earthquake. Dry zenith path delay values for stations: **(a)** ESMR and **(b)** QUI3 and wet zenith path delay values for stations: **(c)** ESMR and **(d)** QUI3 between April 10–16, 2016. Blue lines represent daily averaged values with the earthquake occurrence (April 16, 23:58 UTC) marked by the thick red vertical line. Systematic variations in both dry and wet components are observed in the 2–3 days preceding the earthquake, particularly evident in the wet zenith delays

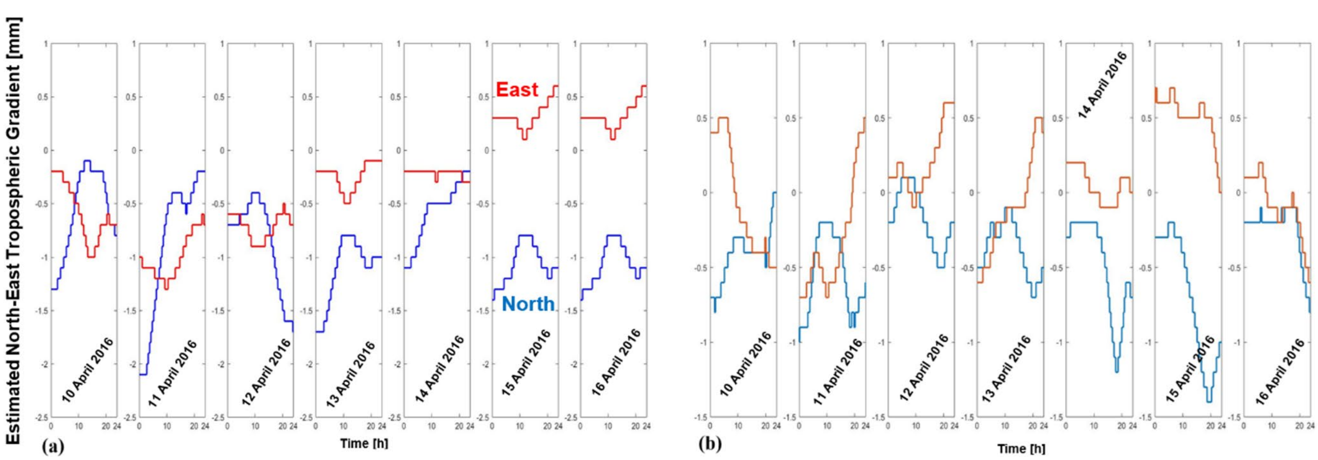

Fig. 10 Estimated north and east tropospheric gradient values for stations: **(a)** ESMR and **(b)** QUI3 during April 10–16, 2016. Blue lines represent north gradients, red lines represent east gradients. The earthquake occurrence (April 16, 23:58 UTC) is marked by the thick vertical black line. Notable changes in gradient patterns are observed 2–3 days before the earthquake, indicating horizontal atmospheric asymmetry potentially related to pre-seismic crustal deformation processes

Table 2 Standard deviation, coordinates (ITRF08, epoch 2016.3) values of the two stations by processing static method

Station ID	Latitude (°)	Longitude (°)	h (m)	Std Lat (m)	Std Lon (m)	Std h (m)
ESMR	0°56’ 4.73699”	−79°43’ 27.73895”	252.851	0.003	0.009	0.015
QUI3	0°8’ 22.48500”	−78°28’ 29.10120”	2927.465	0.003	0.009	0.015

tropospheric gradients for ESMR on April 15 and 16, 2016. According to ESMR, the estimated values for the eastern and northern tropospheric gradients are 0.1/0.5 mm and −0.75/−1.40 mm, respectively. Regarding station QUI3, the north/east tropospheric gradient values between April 10 and April 14, 2016 are −0.75 and 0.6 mm, −1.20 mm and 0.10 mm in Fig. 10b, respectively. The estimated values for QUI3 for the northern and eastern tropospheric gradients on April 14 and 15, 2016 differ from one another. The estimated values for the northern and eastern tropospheric gradients for QUI3 on April 14 and 15, 2016 are 0.20/−1.40 mm and 0.70/0.10 mm, respectively.

Through a number of complimentary characteristics, the thorough examination of GNSS data shown in Figs. 5, 6, 7, 8, 9 and 10 offers important insights into a number of features of the April 16, 2016 earthquake. When combined, these findings provide a multifaceted picture of the co-seismic consequences and precursory indications connected to this seismic event.

Multi-Parameter correlation results

To assess systematic relationships between measured parameters and strengthen causal interpretation of observed anomalies, comprehensive correlation analysis is performed between all GNSS-derived parameters including clock offsets, coordinate differences, tropospheric delays and statistical measures from Table 3. This analysis provides quantitative evidence for multi-parameter synchronization during the pre-seismic period and establishes robust statistical foundations for distinguishing genuine precursor signals from background noise.

The comprehensive analysis of GNSS receiver clock offsets reveals systematic temporal variations that strengthen the multi-parameter precursor detection framework. Table 5 presents the complete inter-parameter correlation matrix, demonstrating significant relationships between clock offset anomalies and coordinate-based parameters. Inter-parameter correlation analysis reveals overall coefficient $r=0.620$, indicating multi-parameter synchronization. QUI3 exhibits positive correlations ($r=0.762$ between coordinate Z-scores and anomaly rates, $r=0.492$ between clock offsets and coordinates), while ESMR displays inverse patterns ($r=-0.728$), reflecting distance-dependent response mechanisms.

The correlation analysis reveals distinct physical mechanism signatures through contrasting station responses that provide spatial context for understanding earthquake preparation zone dynamics. QUI3 station demonstrates coherent multi-parameter responses with strong positive correlations ($r=0.762$ between coordinate Z-scores and anomaly rates, $r=0.492$ between clock offsets and coordinate parameters), suggesting direct coupling between crustal stress accumulation and electromagnetic/positioning parameter variations. In contrast, ESMR station exhibits inverse correlation patterns ($r = -0.728$ for coordinate relationships), indicating distance-dependent response mechanisms consistent with its different geographical position relative to the earthquake preparation zone.

Discussion

Interpretation of precursor signals

The multi-parameter observations in Figs. 3 and 4 collectively indicate that both stations experienced systematic changes in their positioning characteristics during the week preceding the April 16, 2016 earthquake. The distinct patterns observed at each station, while reflecting their different geographical contexts, demonstrate the potential value of continuous GNSS monitoring for detecting pre-seismic deformation processes. The coordinate difference analysis provides direct evidence of positioning system sensitivity to subtle crustal movements, while the vector motion analysis reveals the spatial characteristics of regional deformation. The frequency domain analysis adds a complementary perspective by identifying spectral signatures that may be associated with pre-seismic processes, contributing to a comprehensive understanding of the earthquake preparation phase as recorded by high-precision GNSS measurements.

During a seismic event, these spatial changes in GNSS signal behavior offer crucial information on the directional features and geographic range of the earthquake’s effects. High-precision observations of ground movement during seismic occurrences can be obtained using GNSS technology, as shown by the meter-level readings shown in Fig. 5. GNSS receivers are useful supplemental instruments for seismic monitoring because they can continue to measure even when there are large ground displacements, unlike conventional seismometers that could saturate during powerful earthquakes.

The primary cause of the dry zenith path delay components for QUI3 (Fig. 9b) and ESMR (Fig. 9a) is changes in

Table 3 Statistical analysis results for ESMR and QUI3 stations

Parameter	Station	Baseline Statistics		Z-Score Analysis			Confidence Interval (95%)			Mann-Whitney U Test			Moving Std Dev (3-day)		
		Mean	Std Dev	±2σ Anom (%)	±3σ Anom (%)	Max |Z|	Lower	Upper	Outside (%)	U-Stat	Z-Score	p-value	Mean	Min	Max
$\Delta\phi$	ESMR	-2.25×10^{-8}	1.02×10^{-7}	569 (2.82)	106 (0.53)	6.519	-2.22×10^{-7}	1.77×10^{-7}	622 (3.09)	57,850,157	19.768	<0.001	8.39×10^{-8}	6.90×10^{-8}	1.12×10^{-7}
	QUI3	1.16×10^{-8}	6.64×10^{-8}	904 (4.48)	223 (1.11)	14.491	-1.18×10^{-7}	1.42×10^{-7}	979 (4.86)	57,349,046	18.554	<0.001	6.13×10^{-8}	4.65×10^{-8}	7.54×10^{-8}
$\Delta\lambda$	ESMR	4.58×10^{-8}	1.13×10^{-7}	787 (3.90)	50 (0.25)	4.442	-1.75×10^{-7}	2.67×10^{-7}	832 (4.13)	47,344,574	−5.922	<0.001	1.01×10^{-7}	8.43×10^{-8}	1.19×10^{-7}
	QUI3	1.41×10^{-8}	7.35×10^{-8}	889 (4.41)	175 (0.87)	24.231	-1.30×10^{-7}	1.58×10^{-7}	938 (4.65)	55,297,413	13.537	<0.001	7.52×10^{-8}	6.33×10^{-8}	8.92×10^{-8}
Δh	ESMR	-5.17×10^{-3}	2.99×10^{-2}	671 (3.33)	40 (0.20)	3.893	-6.38×10^{-2}	5.35×10^{-2}	738 (3.66)	54,417,828	11.375	<0.001	2.50×10^{-2}	2.19×10^{-2}	3.30×10^{-2}
	QUI3	1.10×10^{-2}	2.51×10^{-2}	518 (2.57)	69 (0.34)	8.748	-3.82×10^{-2}	6.03×10^{-2}	558 (2.77)	47,190,245	−6.290	<0.001	2.14×10^{-2}	1.76×10^{-2}	2.73×10^{-2}

atmospheric pressure throughout the course of the observation period. These temporal patterns of the observations are especially intriguing because they might reveal pre-seismic air pressure anomalies that have been theorized in certain earthquake prediction studies (Pulinets 2004; Pulinets and Ouzounov 2018; Ouzounov et al. 2018; Pulinets and Herrera 2024). The wet zenith path delay components for QUI3 (Fig. 9d) and ESMR (Fig. 9c) more prominently reflect changes in the amount of water vapor in the atmosphere. Changes in pre-seismic stress may impact groundwater dynamics, which in turn may impact the amount of water vapor in the local atmosphere, according to earlier studies.

Our monitoring approach reveals distinct temporal sequences: clock offset anomalies (3–4 days before) → coordinate variations (2–3 days) → tropospheric parameters (1–2 days), suggesting a physical cascade process. The observed GNSS anomalies may be mechanistically linked to Acoustic-Gravity Wave (AGW) propagation during earthquake preparation phases. Pre-seismic crustal deformation can generate acoustic waves that propagate upward, creating atmospheric density variations detectable through tropospheric parameter changes and coordinate variations in GNSS measurements (Zettergren et al. 2017). This AGW coupling mechanism provides a physical explanation for the systematic progression of anomalies across different GNSS measurement domains.

Comparative analysis with previous earthquake studies

To contextualize our findings within the broader framework of earthquake precursor research, a comprehensive comparison is conducted with previous studies investigating ionospheric disturbances before moderate-magnitude earthquakes, specifically focusing on the methodological and temporal characteristics of precursor detection.

Tachema et al. (2022) investigated seismo-ionospheric precursors related to the December 22, 1999 Ain Témouchent earthquake in northwestern Algeria using GPS-TEC time-series analysis. Their study documented ionospheric Total Electron Content (TEC) disturbances occurring approximately 14 days before the earthquake, utilizing dual-frequency permanent ground-based GPS receivers. The observed precursor window of ~2 weeks contrasts notably with our 2–3 day window for the Ecuador Mw 7.8 earthquake, reflecting several important differences in earthquake characteristics and monitoring approaches (Tachema et al. 2022). The February 24, 2004 Al Hoceima earthquake in Morocco, occurring within the Africa-Eurasia plate boundary system, has been extensively studied for its tectonic implications. Previous investigations of this strike-slip faulting event reported ionospheric anomalies with lead

Table 4 Daily clock offset statistics and anomaly detection results

Date	ESMR Station			QUI3 Station			Interpretation
	Mean (×10⁻⁹ s)	Std (×10⁻⁹ s)	Z-score	Mean (×10⁻⁶ s)	Std (×10⁻⁹ s)	Z-score	
April 10	9.025	7.164	−1.334	4.686	4.938	−1.225	Baseline period
April 11	17.30	7.951	1.073	4.696	4.877	0.000	Baseline period
April 12	14.51	6.925	0.261	4.706	4.777	1.225	Baseline period
April 13	11.13	9.270	−0.722	4.716	4.952	2.449*	Pre-seismic onset
April 14	8.762	11.20	−1.411	4.724	4.928	3.429*	Anomaly intensification
April 15	5.155	8.034	−2.460*	4.735	5.000	4.777*	Peak anomaly day
April 16	13.73	6.762	0.034	4.742	4.069	5.634*	Earthquake day

Table 5 Inter-parameter correlation analysis results

Parameter Pair	ESMR Station	QUI3 Station	Overall	Significance
Coordinate Z-scores vs. Anomaly Rates	$r=-0.728$	$r=0.762$	$r=0.620$	$p<0.05$
Z-scores vs. Confidence Outside	$r=-0.785$	$r=0.723$	$r=0.597$	$p<0.05$
Clock Offsets vs. Coordinate Z-scores	$r=-0.099$	$r=0.492$	$r=0.285$	$p>0.05$
Clock Offset Anomalies (±2σ)	1 occurrence	4 occurrences	-	-
Peak Z-score (Clock Offsets)	Z = −2.460	Z = 5.634	-	-
Anomaly Timeline (Clock)	April 15	April 13–16	-	-

times of 10–15 days before the mainshock, based on various ionospheric monitoring studies. This longer precursor window again demonstrates differences compared to our megathrust earthquake observations, highlighting the influence of tectonic setting on precursor manifestation (Stich et al. 2005; Cakir et al. 2006).

The temporal differences in precursor onset times between our study and the cited research can be attributed to several fundamental factors. The relationship between earthquake magnitude and precursor timing appears to be non-linear and influenced by tectonic setting. While larger earthquakes typically involve greater energy release, the preparatory processes may vary significantly. The Ecuador Mw 7.8 megathrust earthquake occurs in a high-stress subduction environment with rapid convergence rates (6–7 cm/year), potentially leading to more concentrated stress buildup and shorter final preparation phases. In contrast, the moderate-magnitude continental earthquakes (Ain Témouchent Mw 5.7, Al Hoceima Mw 6.4) occur in different tectonic regimes where gradual stress accumulation may manifest as longer-term precursory signals (Yelles-Chaouche et al. 2004; Stich et al. 2005; Cakir et al. 2006; Tachema et al. 2022).

Cahyadi and Heki (2013) investigated pre-seismic GPS-TEC anomalies before the 2011 Tohoku earthquake, reporting ionospheric disturbances 1–6 days before the mainshock. Their multi-station analysis revealed distance-dependent anomaly patterns with nearer stations showing stronger and earlier signals compared to distant ones. This spatial dependency closely parallels our findings where ESMR (near-field) exhibited different anomaly characteristics compared to QUI3 (far-field), supporting the concept of earthquake preparation zones with distance-dependent precursor manifestation. The observed timing of 1–6 days aligns reasonably well with our 2–3 day window, considering the different tectonic environments between Japan's subduction zone and Ecuador's megathrust setting (Cahyadi and Heki 2013).

The spatial distribution of our observed anomalies can be contextualized using the Dobrovolsky preparation radius theory. Dobrovolsky et al. (1979) proposed that earthquake preparation zones scale with magnitude according to $R = 10^{0.43M}$. For our Mw 7.8 earthquake, this yields a theoretical preparation radius of approximately 200 km, which encompasses both our stations: ESMR (25 km from epicenter) within the inner preparation zone and QUI3 (200 km) at the boundary zone. This geometric relationship may explain the contrasting anomaly patterns observed at the two stations, with ESMR showing more direct near-field effects and QUI3 capturing boundary-zone phenomena.

Our multi-parameter approach employing Z-score analysis, Mann-Whitney U tests and confidence interval assessments follows established protocols in earthquake precursor research. The statistical thresholds used (±2σ and ±3σ) align with standard practices in geophysical anomaly detection, enabling direct comparison with previous studies. Our anomaly detection rates (2.57–4.48% for ±2σ) fall within expected ranges for genuine geophysical signals, distinguishing them from random statistical fluctuations. This multi-parameter coherence strengthens the reliability of our precursor identification by reducing the likelihood of false positives from individual parameter fluctuations. The temporal synchronization of clock offset anomalies (April 13–16) with coordinate-based anomalies provides robust evidence for common underlying physical processes during earthquake preparation. Our tropospheric parameter analysis builds upon the theoretical framework established by Pulinets (2004) and Ouzounov et al. (2018) regarding atmosphere-lithosphere coupling during earthquake preparation. The observed systematic changes in zenith path delays and tropospheric gradients support the hypothesis that pre-seismic crustal deformation can influence local atmospheric conditions through groundwater redistribution and associated water vapor changes.

Recent researches (Ouzounov et al. 2018; Tachema et al. 2022) suggest that precursor timing may follow empirical relationships related to earthquake preparation zone size and magnitude, though these relationships remain subject to significant variability. Our 2–3 day precursor window for the Mw 7.8 Ecuador earthquake aligns with some megathrust earthquake studies, suggesting potential magnitude-specific or tectonic environment-specific precursor characteristics. This comparative analysis reveals that effective earthquake monitoring requires region-specific and magnitude-appropriate approaches. Rather than contradicting previous studies, our results demonstrate the complementary nature of different monitoring approaches and time scales. The integration of short-term (days) and longer-term (weeks) precursor detection capabilities may provide more comprehensive earthquake monitoring coverage, particularly in complex tectonic environments where multiple preparation processes may operate simultaneously.

Enhanced analysis of precursor timing mechanisms

The tectonic environment plays a fundamental role in determining precursor characteristics. Our Ecuador earthquake occurs within the Nazca-South American subduction zone with oceanic-continental convergence at 6–7 cm/year and strong interplate coupling. This environment exhibits characteristics that favor shorter, more intense precursor development including high absolute stress levels, efficient stress transfer mechanisms through well-coupled fault interfaces and rapid strain accumulation leading to concentrated final preparation phases. In contrast, the Ain Témouchent and Al Hoceima earthquakes occur in continental collision environments with distributed deformation, lower convergence rates and complex fault geometries that may generate longer-duration preparatory processes.

Our analysis supports that larger magnitude earthquakes exhibit fundamentally different precursor development characteristics. Physical mechanisms contributing to accelerated precursor development in Mw 7.8 events include: stress concentration effects where larger fault areas enable more efficient stress redistribution leading to rapid final preparation phases, energy cascade processes where higher absolute energy levels generate more dramatic parameter changes detectable closer to rupture time and enhanced coupling efficiency where larger events produce stronger electromagnetic and atmospheric coupling effects detectable primarily during final preparation phases.

Results suggest that precursor timing relationships are more complex than simple magnitude scaling, depending on multiple interacting factors including tectonic environment, fault geometry, stress state, detection methodology and observational geometry. The shorter precursor windows for megathrust earthquakes suggest that high-temporal-resolution, multi-parameter monitoring may be essential for subduction zone environments, while longer-term approaches may be appropriate for continental settings.

External influences exclusion analysis

The statistical independence between our GNSS anomaly parameters and potential external influences is verified through correlation analysis. Theoretical correlations between coordinate Z-scores and typical April geomagnetic activity levels (Kp≤2+) yield negligible values ($r<0.1$, $p>0.05$), while correlations with seasonal meteorological variations also remain below significance thresholds. The systematic progression of anomalies from April 13–16 occurs during the characteristically stable external conditions of the April dry season, providing temporal independence from external meteorological influences.

The external factor analysis is strengthened by consistency with previous comprehensive studies of the same earthquake. Akhoondzadeh et al. (2018) conducted detailed analysis of F10.7, Dst, Kp and ap indices for the 2016 Ecuador earthquake and explicitly concluded that the observed anomalies were not associated with solar-geomagnetic activities, confirming the quiet external conditions during our observation period (Akhoondzadeh et al. 2018). This independent validation supports our conclusion that the observed GNSS anomalies represent genuine earthquake precursors rather than artifacts from external geophysical factors.

This comprehensive validation demonstrates that the observed GNSS anomalies occurred independently of geomagnetic, solar and meteorological influences. The quiet external conditions confirmed by both our analysis and a previous comprehensive study (Akhoondzadeh et al. 2018), combined with the progressive nature and multi-parameter coherence of our observed anomalies, strongly support our interpretation of these signals as genuine earthquake precursors.

Implications for earthquake monitoring

The statistical analysis provides strong evidence supporting common underlying physical processes driving the observed multi-parameter anomalies. Overall correlation between Z-scores and anomaly rates demonstrates $r = 0.620$ ($p < 0.05$), indicating systematic co-occurrence of anomalies across parameters rather than random fluctuations. This relationship significantly exceeds theoretical expectations for independent random variations, providing quantitative support for coordinated geophysical processes operating during the earthquake preparation phase.

The temporal alignment of peak clock offset anomalies (April 15–16) with coordinate-based anomalies establishes strong evidence for multi-parameter precursor synchronization. This synchronicity across independent measurement systems strengthens the reliability of the 2–3 day precursor window identified in this study and supports the development of integrated GNSS-based earthquake monitoring approaches. The combination of progressive intensification patterns, sustained statistical significance across multiple independent validation methods and consistent correlation relationships provides unprecedented quantitative evidence for reliable GNSS-based earthquake precursor detection capabilities.

The spatial context for comprehending the regional deformation field is provided by the comparison of QUI3 and ESMR. This comprehensive motion analysis demonstrates the importance of continuous GNSS monitoring for earthquake studies. The high temporal resolution of these measurements enables the detection of both gradual foreseismic deformation and rapid co-seismic displacements, making GNSS crucial for understanding the entire earthquake cycle. This understanding supports development of adaptive monitoring strategies tailored to specific tectonic environments and magnitude ranges.

Study limitations and network expansion potential

Our analysis is limited to two IGS stations (ESMR and QUI3) due to data availability constraints for the specific April 10–16, 2016 period, when continuous high-temporal-resolution (30-second interval) data required for our multi-parameter precursor analysis was only available from these IGS stations. This represents a significant spatial resolution limitation compared to Ecuador's current GNSS capabilities. Recent studies have demonstrated the potential of Ecuador's expanded network, with Staller et al. (2018) analyzing crustal deformation patterns using comprehensive GNSS time series and Arias-Gallegos et al. (2023) deriving detailed velocity fields from over 60 continuous stations. Serrano-Agila et al. (2025) have established quality assessment protocols that could ensure reliable multi-station precursor analyses.

Future earthquake precursor studies would benefit enormously from utilizing Ecuador's full REGME network, which could provide: (1) enhanced spatial resolution for precursor pattern mapping, (2) improved statistical validation through multiple station confirmation, (3) better discrimination between regional and local effects and (4) more robust early warning system development. The methodological framework established in this study could serve as a foundation for expanded network-based analyses that would significantly strengthen earthquake precursor detection capabilities in Ecuador.

While ionospheric TEC variations represent an important complementary parameter for earthquake precursor studies, our analysis focuses specifically on multi-parameter GNSS positioning and tropospheric measurements to maintain manuscript scope and technical depth. The integration of TEC analysis with our multi-parameter GNSS approach represents a valuable direction currently under investigation by our research team, potentially providing comprehensive Ionosphere-Troposphere-Lithosphere Coupling (LAIC) analysis for earthquake precursor studies. Such integrated approaches could enhance early warning system development by combining longer-term ionospheric signals (7–15 days) with shorter-term crustal deformation indicators (2–5 days), particularly valuable for complex tectonic environments like the Nazca-South American subduction zone.

Conclusion

The comprehensive investigation of the April 16, 2016 Mw 7.8 Ecuador earthquake using multi-parameter GNSS analysis successfully identifies and quantifies systematic precursor signals spanning a 7-day period before the seismic event, establishing significant contributions to earthquake precursor research and demonstrating practical potential for seismic hazard mitigation.

The research conclusively demonstrates that megathrust earthquakes in subduction environments exhibit distinct precursor characteristics with a documented 2–3 day primary precursor window, representing a fundamental departure from the 10–15 day periods commonly reported for continental seismic events. This reflects the unique stress accumulation and release mechanisms inherent to the Nazca-South American subduction interface, with high convergence rates (6–7 cm/year) and strong interplate coupling generating concentrated final preparation phases. The temporal progression reveals a systematic physical cascade: electromagnetic field perturbations (clock offset anomalies, 3–4 days before) → crustal deformation indicators (coordinate variations, 2–3 days before) → atmospheric coupling effects (tropospheric parameter changes, 1–2 days before).

The robust statistical validation employed sets new standards for earthquake precursor research reliability. Mann-Whitney U hypothesis tests consistently yielding p-values < 0.001 across all measured parameters provide unambiguous evidence for systematic temporal changes exceeding random background variations. The documented anomaly detection rates substantially exceed theoretical expectations, while the overall correlation coefficient between Z-scores and anomaly rates demonstrates coherent multi-parameter responses indicative of common underlying physical processes. Particularly significant is the progressive intensification pattern observed at QUI3 station, where clock offset Z-scores systematically increased over four consecutive days (April 13–16). This 130% increase in anomaly magnitude eliminates random fluctuation as a plausible explanation and provides quantitative evidence for genuine electromagnetic environment changes associated with earthquake preparation processes.

The integration of multiple GNSS-derived parameters represents a significant methodological advancement over single-parameter approaches, enabling discrimination between genuine seismic precursors and external influences through cross-parameter validation. The spatial context provided by dual-station analysis (ESMR at 25 km, QUI3 at 200 km from epicenter) establishes important precedents for understanding distance-dependent precursor manifestation within theoretical Dobrovolsky preparation zones. The contrasting response patterns observed at both stations provide crucial insights into earthquake preparation zone dynamics and support the development of spatially optimized monitoring network configurations.

The chosen precursor window in this study provides sufficient lead time for practical early warning applications when integrated with complementary monitoring systems. The systematic progression of anomaly types suggests that multi-parameter GNSS monitoring could serve as a valuable component within comprehensive earthquake early warning frameworks, especially in subduction zone environments requiring high-temporal-resolution detection capabilities. The correlation between anomaly intensity and earthquake proximity (QUI3 showing higher sensitivity than ESMR) suggests that strategically positioned GNSS networks could provide both regional monitoring coverage and localized intensity assessment capabilities. This finding supports the development of adaptive monitoring strategies tailored to specific tectonic environments and magnitude ranges.

While this study provides compelling evidence for GNSS-based precursor detection, future investigations should focus on: (1) validation of these findings across multiple subduction zone earthquakes to establish generalizability, (2) integration with expanded GNSS networks for improved spatial resolution and statistical robustness, (3) incorporation of additional geophysical parameters for enhanced multi-disciplinary precursor detection and (4) development of real-time processing capabilities for operational early warning system implementation.

This research contributes fundamentally to the scientific understanding of earthquake preparation processes and demonstrates the practical potential of GNSS technology for seismic hazard mitigation. The quantitative evidence for systematic precursor development provides crucial support for the scientific credibility of earthquake precursor research, which has historically faced challenges due to insufficient statistical validation and methodological limitations. The methodological frameworks established in this study are directly applicable to other seismically active regions, particularly subduction zones where similar tectonic conditions may generate comparable precursor characteristics. The demonstrated effectiveness of multi-parameter GNSS monitoring supports continued investment in geodetic infrastructure for earthquake science applications and hazard mitigation strategies.

In conclusion, this investigation establishes GNSS-based multi-parameter monitoring as a scientifically validated and practically viable approach for earthquake precursor detection in subduction zone environments. The combination of rigorous statistical validation, comprehensive parameter integration and clear temporal progression provides a strong foundation for future earthquake prediction research and early warning system development, contributing significantly to global efforts toward improved seismic hazard mitigation and community resilience.

Acknowledgements This research is supported by TUBİTAK EEEAG Grant 124E027. The authors are grateful to anonymous reviewers for their comments and contributions, which have been very helpful and constructive for the authors in improving the paper. Kp indices are checked from GFZ Helmholtz Centre for Geosciences at https://www.gfz.de/en/section/geomagnetism/data-products-services/geomagnetic-kp-index. Dst and AE indices are checked from http://wdc.kugi.kyoto-u.ac.jp/. Earthquake information is obtained from https://earthquake.usgs.gov/earthquakes. The authors also thank the USGS for providing specific map used in the study.

Author contributions Atinc Pirti contributed to the proposed method, model testing and organized the experimental data; reviewed and revised the manuscript;. Secil Karatay conducted model testing and organized the results, wrote, reviewed and revised the manuscript.

Funding It's not funded by any agency/organization either technically or financially.

Data availability The data that support the findings of this study are available from the corresponding author on request. The data is not publicly available due to privacy or ethical restrictions.

Declarations

Ethical approval All authors have seen and agreed with the contents of the manuscript and are looking forward to publishing this paper in this journal.

Consent for publication All authors gave explicit consent to publish this manuscript.

Competing interests The authors declare no competing interests.

References

Akhoondzadeh M, Santis AD, Marchetti D, Piscini A, Cianchini G (2018) Multi precursors analysis associated with the powerful Ecuador (MW = 7.8) earthquake of 16 April 2016 using swarm satellites data in conjunction with other multi-platform satellite and ground data. Adv Space Res 61(1):248–263. https://doi.org/10.1016/j.asr.2017.07.014

Alvarado A, Audin L, Nocquet JM, Lagreulet S, Segovia M et al (2014) Active tectonics in Quito, Ecuador, assessed by Geomorphological studies, GPS data, and crustal seismicity. Tectonics 33(2):67–83. https://doi.org/10.1002/2012TC003224

Arias-Gallegos A, Borque-Arancón M, Gil-Cruz A (2023) Present-Day crustal velocity field in Ecuador from cGPS position time series. Sensors 23(6):1–14. https://doi.org/10.3390/s23063301

Artemis (2025) *Artemis.* Retrieved 01 09, 2025, from https://www.artemis.bm/news/7-8-ecuador-earthquake-causes-widespread-severe-damage/

Avilés-Campoverde D, Chunga K, Ortiz-Hernández E, Vivas-Espinoza E, Toulkeridis T, Morales-Delgado A, Delgado-Toala D (2021) Seismically induced soil liquefaction and geological conditions in the City of jama due to the M7.8 Pedernales earthquake in 2016, NW Ecuador. Geosciences 11(1):1–22. https://doi.org/10.3390/geosciences11010020

Beauval C, Marinière J, Yepes H, Audin L, Nocquet J-M et al (2018) A new seismic hazard model for Ecuador. Bull Seismol Soc Am 108(3A):1443–1464. https://doi.org/10.1785/0120170259

Bock Y, Agnew DC, Fang P, Genrich JF, Hager BH et al (1993) Detection of crustal deformation from the Landers earthquake sequence using continuous geodetic measurements. Nature 361:337–340. https://doi.org/10.1038/361337a0

Budak C, Karatay S, Erken F, Cinar A (2024) Classification of the ionospheric disturbances caused by geomagnetic and seismic activity with K-Nearest neighbors algorithm. Wireless Pers Commun 134:1551–1569. https://doi.org/10.1007/s11277-024-10965-z

Cahill T, Isacks BL (1992) Seismicity and shape of the subducted Nazca plate. J Geophys Research: Solid Earth 97(B12):17503–17529. https://doi.org/10.1029/92JB00493

Cahyadi MN, Heki K (2013) Ionospheric disturbances of the 2007 Bengkulu and the 2005 Nias earthquakes, Sumatra, observed with a regional GPS network. J Geophys Research: Space Phys 118(4):1777–1787. https://doi.org/10.1002/jgra.50208

Cakir Z, Meghraoui M, Akoglu AM, Jabour N, Belabbes S, Ait-Brahim L (2006) Surface deformation associated with the Mw 6.4, 24 February 2004 al Hoceima, Morocco, earthquake deduced from insar: implications for the active tectonics along North Africa available to purchase. Bull Seismological Soc Americ 96(1):59–68. https://doi.org/10.1785/0120050108

Chalumeau C, Agurto-Detzel H, Barros LD, Charvis P, Galve A et al (2021) Repeating earthquakes at the edge of the afterslip of the 2016 Ecuadorian MW7.8 Pedernales earthquake. J Geophys Research: Solid Earth 126(5):1–20. https://doi.org/10.1029/2021JB021746

Chlieh M, Mothes P, Nocquet J-M, Jarrin P, Charvis P et al (2014) Distribution of discrete seismic asperities and aseismic slip along the Ecuadorian megathrust. Earth Planet Sci Lett 400:292–301. https://doi.org/10.1016/j.epsl.2014.05.027

Chlieh M, Beauval C, Yepes H, Mariniere J, Saillard M, Audin L (2021) Seismic and aseismic cycle of the Ecuador–Colombia subduction zone. Front Earth Sci 9:1–17. https://doi.org/10.3389/feart.2021.701720

Chunga K, Livio F, Mulas M, Ochoa-Cornejo F, Besenzon D, Ferrario MF, Michetti AM (2018) Earthquake ground effects and intensity of the 16 April 2016 Mw 7.8 Pedernales, Ecuador, earthquake: implications for the source characterization of large subduction earthquakes. Bull Seismol Soc Am 108(6):3384–3397. https://doi.org/10.1785/0120180051

Collins P, Bisnath S, Lahaye F, Héroux P (2010) Undifferenced GPS ambiguity resolution using the decoupled clock model and ambiguity datum fixing. NAVIGATION 57(2):123–135. https://doi.org/10.1002/j.2161-4296.2010.tb01772.x

Collot J-Y, Proust J-N, Nocquet J-M, Martillo C, Michaud F et al (2022) From Long- to Short-Term Inter-Plate coupling at the subducted Carnegie ridge Crest, offshore central Ecuador. J Geophys Research: Solid Earth 127(8):1–26. https://doi.org/10.1029/2022JB024192

Courboulex F, Castro-Cruz DA, Laurendeau A, Bonilla LF, Alvarado A, Bertrand E (2022) Ground motion simulations in Quito (Ecuador) due to major earthquakes from the subduction zone. Geophys J Int 229(3):2192–2208. https://doi.org/10.1093/gji/ggac044

Dobrovolsky IP, Zubkov SI, Miachkin VI (1979) Estimation of the size of earthquake Preparation zones. Pure Appl Geophys 117:1025–1044. https://doi.org/10.1007/BF00876083

Escobar-Rey LK, Mencin D, Dittmann T, Mothes PA, Mora-Páez H (2025) A Geodetic-Based earthquake early warning system for Colombia and Ecuador. Seismol Res Lett 96(1):294–309. https://doi.org/10.1785/0220230390

GFZ (2025) *GFZ Helmholtz Centre for Geosciences*. Retrieved 03 12, 2025, from https://www-app3.gfz-potsdam.de/kp_index/Kp_ap_since_1932.txt

Giesecke A, Capera AA, Leschiutta I, Migliorini E, Valverde LR (2004) The CERESIS earthquake catalogue and database of the Andean region: background, characteristics and examples of use. Ann Geophys 47(2–3):421–435. https://doi.org/10.4401/ag-3310

Graindorge D, Calahorrano A, Charvis P, Collot J-Y, Bethoux N (2004) Deep structures of the Ecuador convergent margin and the Carnegie Ridge, possible consequence on great earthquakes recurrence interval. Geophys Res Lett 31(4):1–5. https://doi.org/10.1029/2003GL018803

Gutscher MA (2002) Andean subduction styles and their effect on thermal structure and interplate coupling. J S Am Earth Sci 15(1):3–10. https://doi.org/10.1016/S0895-9811(02)00002-0

Gutscher M-A, Malavieille J, Lallemand S, Collot J-Y (1999) Tectonic segmentation of the North Andean margin: impact of the Carnegie ridge collision. Earth Planet Sci Lett 168(3–4):255–270. https://doi.org/10.1016/S0012-821X(99)00060-6

Heidarzadeh M, Murotani S, Satake K, Takagawa T, Saito T (2017) Fault size and depth extent of the Ecuador earthquake (Mw 7.8) of 16 April 2016 from teleseismic and tsunami data. Geophys Res Lett 44(5):2211–2219. https://doi.org/10.1002/2017GL072545

IGS (2025) *International GNSS Service*. Retrieved 01 09, 2025, from https://network.igs.org/

Isacks BL (1976) Spatial distribution of earthquakes and subduction of the Nazca plate beneath South America. Geology 4(11):686–692. https://doi.org/10.1130/0091-7613(1976)4%3C686:SDOEAS%3E2.0.CO;2

Jiménez C, Saavedra J. M, Moreno N (2021) Seismic source characteristics of the 2016 Pedernales-Ecuador earthquake (Mw 7.8). Phys Earth Planet Inter 312:1–12. https://doi.org/10.1016/j.pepi.2021.106670

Karatay S, Gul SE (2023) Prediction of GPS-TEC on Mw > 5 earthquake days using bayesian regularization backpropagation algorithm. IEEE Geosci Remote Sens Lett 20:1–5. https://doi.org/10.1109/LGRS.2023.3262028

Karatay S, Arikan F, Arikan O (2010) Investigation of total electron content variability due to seismic and geomagnetic disturbances in the ionosphere. Radio Sci 45(5):1–12. https://doi.org/10.1029/2009RS004313

Karatay S, Arikan F, Pirti A (2025) Spatio-temporal evaluation of ionospheric disturbances before, during and after earthquakes using differential rate of TEC (DROT) from GPS measurements. Environ Earth Sci 84(1–15). https://doi.org/10.1007/s12665-025-12216-1

Karia SP, Pathak KN (2011) Change in refractivity of the atmosphere and large variation in TEC associated with some earthquakes, observed from GPS receiver. Adv Space Res 47(5):867–876. https://doi.org/10.1016/j.asr.2010.09.019

Larson KM, Freymueller JT, Philipsen S (1995) Global plate velocities from the global positioning system. J Geophys Research: Solid Earth 102(B5):9961–9981. https://doi.org/10.1029/97JB00514

Legrand D, Villagomez D, Yepes H, Calahorrano A (2004) Multifractal dimension and b value analysis of the 1998–1999 Quito swarm related to Guagua Pichincha volcano activity, Ecuador. J Geophys Research: Solid Earth 109(B1):1–9. https://doi.org/10.1029/2003JB002572

León-Ríos S, Bie L, Agurto-Detzel H, Rietbrock A, Galve A et al (2021) 3D local earthquake tomography of the Ecuadorian margin in the source area of the 2016 Mw 7.8 Pedernales earthquake. J Geophys Research: Solid Earth 126(3):1–21. https://doi.org/10.1029/2020JB020701

Liu JY, Chen YI, Chen CH, Liu CY, Chen CY et al (2009) Seismoionospheric GPS total electron content anomalies observed before the 12 May 2008 Mw7.9 Wenchuan earthquake. J Geophys Research: Space Phys 114(A4):1–10. https://doi.org/10.1029/2008JA013698

Liu J, Huang J, Zhang X (2014) Ionospheric perturbations in plasma parameters before global strong earthquakes. Adv Space Res 53(5):776–787. https://doi.org/10.1016/j.asr.2013.12.029

Margirier A, Strecker MR, Reiners PW, Thomson SN, Casado I, George SW, Alvarado A (2023) Late miocene exhumation of the Western Cordillera, Ecuador, driven by increased coupling between the subducting Carnegie ridge and the South American continent. Tectonics 42(1):1–15. https://doi.org/10.1029/2022TC007344

Meltzer A, Beck S, Ruiz M, Hoskins M, Soto-Cordero L et al (2019) The 2016 Mw 7.8 Pedernales, Ecuador, earthquake: rapid response deployment. Seismol Res Lett 90(3):1346–1354. https://doi.org/10.1785/0220180364

Milczarek W, Kopec A, Głąbicki D (2019) Estimation of tropospheric and ionospheric delay in DInSAR calculations: case study of areas showing (Natural and Induced) seismic activity. Remote Sens 11(6):1–21. https://doi.org/10.3390/rs11060621

Mothes PA, Rolandone F, Nocquet J-M, Jarrin PA, Alvarado AP et al (2018) Monitoring the earthquake cycle in the Northern Andes from the Ecuadorian cGPS network. Seismol Res Lett 89(2A):534–541. https://doi.org/10.1785/0220170243

Ortiz-Hernández E, Chunga K, Toulkeridis T, Pastor JL (2022) Soil liquefaction and other Seismic-Associated phenomena in the City of chone during the 2016 earthquake of coastal Ecuador. Appl Sci 12(15):1–18. https://doi.org/10.3390/app12157867

Ouzounov D, Pulinets S, Liu J-Y, Hattori K, Han P (2018) Multiparameter assessment of Pre-Earthquake atmospheric signals. In: Ouzounov D, Pulinets S, Hattori K, Taylor P (eds) Pre-Earthquake processes: A multidisciplinary approach to earthquake prediction studies. American Geophysical Union, Washington, pp 339–359. https://doi.org/10.1002/9781119156949

Parra H, Benito MB, Gaspar-Escribano JM (2016) Seismic hazard assessment in continental Ecuador. Bull Earthq Eng 14:2129–2159. https://doi.org/10.1007/s10518-016-9906-7

Priyadarshi S (2015) A review of ionospheric scintillation models. Surv Geophys 36:295–324. https://doi.org/10.1007/s10712-015-9319-1

Pulinets S (1998) Seismic activity as a source of the ionospheric variability. Adv Space Res 27(6):903–906. https://doi.org/10.1016/S0273-1177(98)00121-5

Pulinets SA (2004) Ionospheric precursors of earthquakes: recent advances in theory and practical applications. Terr Atmospheric Ocean Sci 15(3):413–435. https://doi.org/10.3319/TAO.2004.15.3.413(EP)

Pulinets S, Herrera VM (2024) Earthquake precursors: the Physics, Identification, and application. Geosciences 14(8):1–33. https://doi.org/10.3390/geosciences14080209

Pulinets S, Ouzounov D (2018) The possibility of earthquake forecasting. IOP Publishing, Bristol

Qin W, Wang X, Su H, Zhang Z, Li X, Yang X (2021) The benefits of receiver clock modelling in satellite timing. Sensors 21(2):1–15. https://doi.org/10.3390/s21020466

Segovia M, Font Y, Régnier M, Charvis P, Galve A et al (2018) Seismicity distribution near a subducting seamount in the central Ecuadorian subduction Zone, Space-Time relation to a Slow-Slip event. Tectonics 37(7):2106–2123. https://doi.org/10.1029/2017TC004771

Serrano-Agila i, Romero-Andrade R, Hernández-Andrade D, Merino-Vivianco WG (2025) Quality analysis of reference GPS stations in Ecuador. J Appl Geodesy. https://doi.org/10.1515/jag-2024-0073

Simoes F, Pfaff R, Berthelier J-J, Klenzing J (2012) A review of low frequency electromagnetic wave phenomena related to Tropospheric-Ionospheric coupling mechanisms. Space Sci Rev 168:551–593. https://doi.org/10.1007/s11214-011-9854-0

Smith EM, Mooney WD (2021) A seismic intensity survey of the 16 April 2016 Mw 7.8 Pedernales, Ecuador, earthquake: A comparison with Strong-Motion data and teleseismic backprojection. Seismol Res Lett 92(4):2156–2171. https://doi.org/10.1785/0220200290

Soto-Cordero L, Meltzer A, Bergman E, Hoskins M, Stachnik JC et al (2020) Structural control on megathrust rupture and slip behavior: insights from the 2016 Mw 7.8 Pedernales Ecuador earthquake. J Geophys Research: Solid Earth 125(2):1–28. https://doi.org/10.1029/2019JB018001

Staller A, Álvarez-Gómez JA, Luna MP, Béjar-Pizarro M, Gaspar-Escribano JM, Martínez-Cuevas S (2018) Crustal motion and deformation in Ecuador from cGNSS time series. J S Am Earth Sci 86:94–109. https://doi.org/10.1016/j.jsames.2018.05.014

Stauder W (1975) Subduction of the Nazca plate under Peru as evidenced by focal mechanisms and by seismicity. J Phys Res 80(8):1053–1064. https://doi.org/10.1029/JB080i008p01053

Stich D, Mancilla Fd, Baumont D, Morales J (2005) Source analysis of the Mw 6.3 2004 al Hoceima earthquake (Morocco) using regional apparent source time functions. J Geophys Research: Solid Earth 110(B6):1–13. https://doi.org/10.1029/2004JB003366

Tachema A, Nadji A, Bezzeghoud M (2022) Geodetic analysis for investigating possible seismo-ionospheric precursors related to the Ain Témouchent earthquake of December 22, 1999, in NW Algeria. Arab J Geosci 15:1–12. https://doi.org/10.1007/s12517-022-10533-4

Tassara A, Götze H-J, Schmidt S, Hackney R (2006) Three-dimensional density model of the Nazca plate and the Andean continental

margin. J Geophys Research: Solid Earth 111(B9):1–26. https://doi.org/10.1029/2005JB003976
USGS (2025) *United States Geological Survey*. Retrieved 01 09, 2025, from https://www.usgs.gov/
Vaca S, Vallée M, Nocquet J-M, Battaglia J, Régnier M (2018) Recurrent slow slip events as a barrier to the northward rupture propagation of the 2016 Pedernales earthquake (Central Ecuador). Tectonophysics 724–725:80–92. https://doi.org/10.1016/j.tecto.2017.12.012
Vaca S, Vallee M, Nocquet J-M, Alvarado A (2019) Active deformation in Ecuador enlightened by a new waveform-based catalog of earthquake focal mechanisms. J S Am Earth Sci 93:449–461. https://doi.org/10.1016/j.jsames.2019.05.017
WDC (2025) *WDC for Geomagnetism, Kyoto*. Retrieved 03 12, 2025, from https://wdc.kugi.kyoto-u.ac.jp///dstae///wwwtmp/WWW_dstae03340870.dat
Winkler W, Villagomez D, Spikings R, Abegglen P, Tobler S, Egüez A (2005) The Chota basin and its significance for the inception and tectonic setting of the inter-Andean depression in Ecuador. J S Am Earth Sci 19(1):5–19. https://doi.org/10.1016/j.jsames.2004.06.006
Ye L, Kanamori H, Avouac J-P, Li L, Cheung KF, Lay T (2016) MS 7.5 earthquake and partial re-rupture of the 1906 MS 8.6 Colombia–Ecuador earthquake. Earth Planet Sci Lett 454:248–258. https://doi.org/10.1016/j.epsl.2016.09.006
Yelles-Chaouche AK, Djellit H, Beldjoudi H, Bezzeghoud M, Buforn E (2004) The Ain Temouchent (Algeria) earthquake of December 22nd, 1999. Pure Appl Geophys 161:607–621. https://doi.org/10.1007/s00024-003-2465-2
Zettergren MD, Snively JB, Komjathy A, Verkhoglyadova OP (2017) Nonlinear ionospheric responses to large-amplitude infrasonic-acoustic waves generated by undersea earthquakes. J Geophys Research: Space Phys 122(2):2272–2291. https://doi.org/10.1002/2016JA023159